Catalysis Science & Technology

Accepted Manuscript

ROYAL SOCIETY OF CHEMISTRY

www.rsc.org/catalysis

Catalysis Science & Technology

MINIREVIEW

Structural Design of TiO_2-based Photocatalyst for H_2 Production and Degradation Applications

Minmin Gao,[a] Liangliang Zhu,[a] Weili Ong,[a] Jing Wang[a] and Ghim Wei Ho*[a,b,c]

, they arweReceived 00th January 20xx,
Accepted 00th January 20xx

DOI: 10.1039/x0xx00000x

www.rsc.org/

TiO_2-based photocatalyst being inexpensive and abundant in conjunction with high photostability and environmental friendly characteristics makes it the most extensively studied photocatalytic material for hydrogen production and pollutant degradation. However, its existing issues such as wide bandgap, high overpotential and rapid recombination of photogenerated carriers limit its photocatalytic properties. The opportunities for structural development of TiO_2 nanomaterial towards highly efficient and pragmatic photocatalysis applications are evidently plentiful. Hence in this review, we will look into critical structural engineering strategies that endow favorable physicochemical properties such as improved light absorption, photostability, charge-carrier dynamics, increase surface area etc. that benefit photocatalysis functionalities. Amongst the various structural engineering constitutions, we will be covering the most prevalent and elegant core-shell and hierarchical structural designs that rationally combine the advantages of structural manipulation and multi-material composition engineering. This review aims to provide a comprehensive and contemporary overview as well as a guide of the development of new generation TiO_2 based photocatalysts via structural design for improved solar energy conversion technologies.

1. Introduction

With globalization, industrialization and manufacturing is expanding at an alarming rate in the past century, and that has caused some serious problems to the world's population. The supplies of natural energy sources such as oil and gas are depleted faster than expected and will be emptied within the next 50 years. The extensive use of these energy sources has also produced tonnes of wastes polluting the environment and damaging/altering/affecting the climatic conditions. This has brought about a need for renewable sources of clean energy, and also technologies capable of cleaning the environment.[1] Photocatalysts can be the answer to this calamity that is staring mankind in the face. Under the lucent sunlight, solar energy can be absorbed by the photocatalyst to produce hydrogen (H_2) from photocatalytic water splitting[2] and also degrade organic pollutants[3], paving the way to a clean and renewable source of energy in a cleaner environment.

TiO_2 is a photocatalytic material that has been used for a long time.[4] It is stable, non-toxic, environmentally friendly, cheap and easily synthesized at low temperatures.[2, 5,6] However, it has a wide bandgap, hence limiting its photocatalytic functionality to the UV region of the spectrum. Nonetheless, TiO_2 based photocatalysts are still the most extensively studied materials for the photocatalytic production of H_2 and degradation of pollutants. The enhancement of TiO_2 materials for photocatalytic application lies heavily on the catalyst design and hence warrants a fundamental understanding of all the key objectives of various structural designs for photocatalysis.[7,8] Here, we will review the various structural engineering strategies employed to overcome the drawbacks of TiO_2 for improved photoactivity. The review will cover the least to the most elaborate structural design i.e. basic nanoscale structures, core-shell structures and lastly the hierarchical structures. We will focus our attention on the effects of various structural designs on the chemical and physical properties of TiO_2 ranging from light absorption, surface area, charge-carrier dynamics to photostability. Our goal is to provide a comprehensive background towards rational structural engineering of photocatalysts and provide a guide for future structural design of nanoscale catalyst for photocatalysis H_2 production and degradation applications.

Photocatalytic Reactions on TiO_2 When TiO_2 is illuminated with UV light, the absorbed photons excites the negatively-charged electrons from the valence band (VB) to the conduction band (CB), leaving behind a positively-charge hole in the VB as shown by the following expression:

$$TiO_2 + h\upsilon \rightarrow TiO_2 (e^-) + TiO_2 (h^+) \quad (1)$$

A portion of the photogenerated electrons and holes will undergo recombination in the bulk and at the surface.[9] However, the electrons and holes that managed to reach the surface of TiO_2 without recombination will reduce and oxidize the reactants

Department of Electrical and Computer Engineering, National University of Singapore, 4 Engineering Drive 3, Singapore 117583.
Engineering Science Programme, National University of Singapore, 9 Engineering Drive 1, Singapore 117575.
*Institute of Materials Research and Engineering, A*STAR (Agency for Science, Technology and Research), 3 Research Link, Singapore 117602.*

adsorbed on the TiO_2 surface. The reduction and oxidation reactions are the basis of photocatalytic H_2 production and photodegradation of organic pollutants respectively (Fig. 1). For water splitting, the CB level should be more negative than the redox potential of H^+/H_2, while the VB level should be more positive than the redox potential of O_2/H_2O. The photogenerated holes oxidise H_2O to form O_2 gas while the electrons reduce the H^+ ions to produce H_2 as shown by Eq. (2) and (3) respectively. In the photodegradation of organic compounds, the generated electrons react with dissolved oxygen molecules and produce oxygen peroxide radicals (Eq. (4)), while the positively charged holes (h^+) react with OH^- derived from H_2O to form hydroxyl radicals $OH^\bullet$ (Eq. (5) and (6)). $O_2^{\bullet-}$ and $OH^\bullet$ are powerful oxidizing agents capable of degrading most pollutants.[10, 11] The organic compounds can be photodegraded by the $O_2^{\bullet-}$ and $OH^\bullet$ radicals to CO_2, H_2O, or other mineralization (Eq. (7)).

$$4h^+ + 2H_2O \rightarrow O_2 + 4H^+ \quad (2)$$

$$2e^- + 2H^+ \rightarrow H_2 \quad (3)$$

$$e^- + O_2 \rightarrow O_2^{\bullet-} \quad (4)$$

$$h^+ + OH^- \rightarrow OH^\bullet \quad (5)$$

$$h^+ + H_2O \rightarrow OH^\bullet + H^+ \quad (6)$$

$$O_2^{\bullet-} \text{ or } OH^\bullet + \text{organic pollutants} \rightarrow \text{degradation products} \quad (7)$$

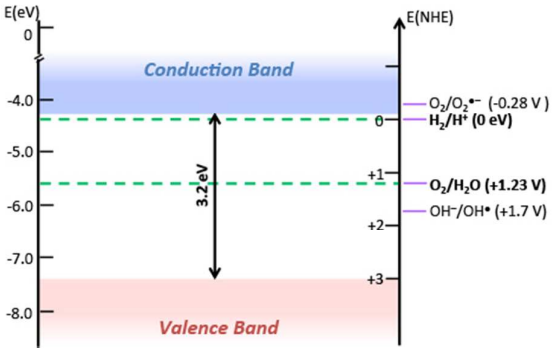

Fig. 1 Schematic representation of the position of CB and VB of TiO_2 and the redox potentials vs NHE at pH 0.

2. Basic Structures of TiO_2

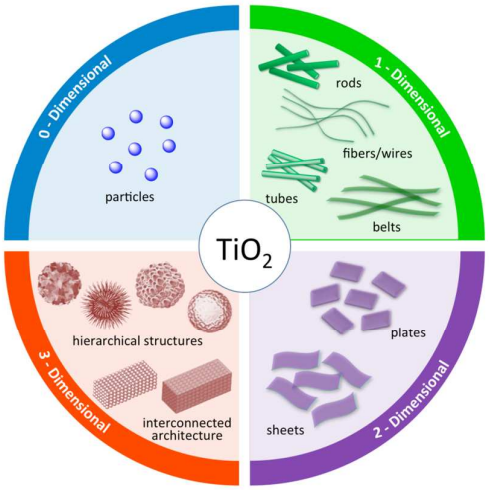

Fig. 2 Schematic diagram of TiO_2 nanostructures according to structural dimensionality.

Many studies have focused on modifying the structures of TiO_2 in nanoscale in order to improve its photocatalytic activities. Fig. 2 shows that nanostructured TiO_2 can exist in various dimensions and morphologies namely zero-dimensional TiO_2 nanoparticles; one-dimensional TiO_2 nanofibers, nanorods, nanowires, nanobelts and nanotubes; two-dimensional TiO_2 nanosheets and nanoplates; and three-dimensional hierarchical and interconnected architectures. These TiO_2 materials of various morphologies do not only improve their photocatalytic properties, but also provide suitable platforms to incorporate other materials such as noble metals,[12, 13-18] transition metals or metal oxides,[19-27] carbon-based materials[28-34] and semiconductors[1, 35-39] for maximizing the photocatalytic efficiency.

There are a few parameters of TiO_2 basic structures that affect the photocatalysis performance which include size, crystallinity, surface to volume ratio and surface chemistry. Optimizing the size of TiO_2 nanoparticles has shown to maximize photocatalytic activities due to their specific size-related properties.[40] The energy band structure becomes discrete for nanometer-scale TiO_2 with its photophysical, photochemical, and surface properties quite different from those of the bulk counterpart due to the quantum size effect.[41] Moreover, smaller photocatalysts reduce electron–hole recombination due to shorter charge transfer distances.[42] The diffusion length of charge carriers has to be longer than the particle size to achieve efficient charge-carrier dynamics. The size-dependent stability of various TiO_2 phases have been reported.[4, 43] The TiO_2 rutile structure is relatively stable in nanoparticles larger than 35 nm; while the anatase structure in nanoparticles larger than 11 nm.[44, 45] On the other hand, the photocatalytic activity is compromised when the nanoparticles are decreased to less than several nanometers due to the dominant electron–hole recombination on the TiO_2 surfaces.[43] Moreover, TiO_2 of higher crystallinity is adopted to facilitate photogenerated charge transfer. Therefore, calcination at appropriate ambient and temperature is often carried out to improve the crystallinity and hence induce lower defect density.

Furthermore, a higher surface to volume ratio of nanostructured materials can help to increase photocatalytic efficiency. A larger surface area increases the number of surface sites available to catalyze the reaction, thus enhancing reactant adsorption and product desorption. Compared to the most common nanostructured TiO_2, such as the commercial TiO_2 nanoparticles (P25), TiO_2 with modified morphologies, such as nanotubes,[46-49] nanofibers,[50, 51] nanorods,[52-55] foams,[56, 57] and mesoporous structures[58-61] have larger surface area. It has been demonstrated that the photoconversion efficiency of TiO_2 nanotubes is almost twice that of spherical nanoparticles.[62] However, large surface with dangling bonds may have different potential states which cause it to act as a recombination center of the excited carriers.[63] Therefore, it is also possible for an increase in the surface area which leads to a decrease in the photocatalytic activity.

In addition, two-dimensinal nanoplates and nanosheets structures have also been explored for improved photocatalytic activity by maximizing active facets of TiO_2. Both theoretical and experimental studies indicate that the {001} of anatase TiO_2 is much more reactive than the thermodynamically stable {101} facet [64, 65] Yang *et al.*[66] developed a method to synthesize high-purity anatase TiO_2

single crystals with high percentage (47%) of {001} facets using hydrofluoric acid as a morphology controlling agent. Subsequently, syntheses of sheet-like anatase TiO_2 single crystals with as much as 90% exposed {001} facets have been demonstrated[67-69] Surface area is another important parameter in optimizing the number of reaction sites available for photocatalysis. Thus, increasing both the surface area and active crystal facet are considered for design of efficient photocatalysts. Hu *et al.*[70] reported ultrathin highly active {001} facet and a high specific surface area (162.4 m^2 g^{-1}) TiO_2 nanosheet superstructures, which has shown two times increase in photodegradation efficiency as compared to P25.

Other three-dimensional TiO_2 structures based on intrinsic shape-dependent properties, such as hollow structures,[71, 72 73-76] interconnected structures,[77, 78, 28, 79, 80] and hierarchical superstructures[81-84] built up from lower-dimensional building blocks have also been reported as efficient photocatalyst. These structures not only possess a high surface area to volume ratio due to the formation of voids amongst the nanobuilding blocks[85], but also possess unique optical and carrier transfer properties which will be discussed in detail later. A new generation photocatalysts based on nanoscale structural manipulation is of particular interest as many of these architectures have distinctive physicochemical properties favorable for photocatalysis applications. Amongst the structural engineering strategies, core-shell and hierarchical structuring of photocatalyst is a prevailing approach for overcoming the drawbacks of pure TiO_2 in photocatalysis. Hereafter, we will be focusing on structural designs and functions of core-shell and hierarchical TiO_2 based-nanostructures for photocatalysis and provide an overview of designing next generation highly efficient TiO_2-based photocatalysts.

3. Core-Shell Structures

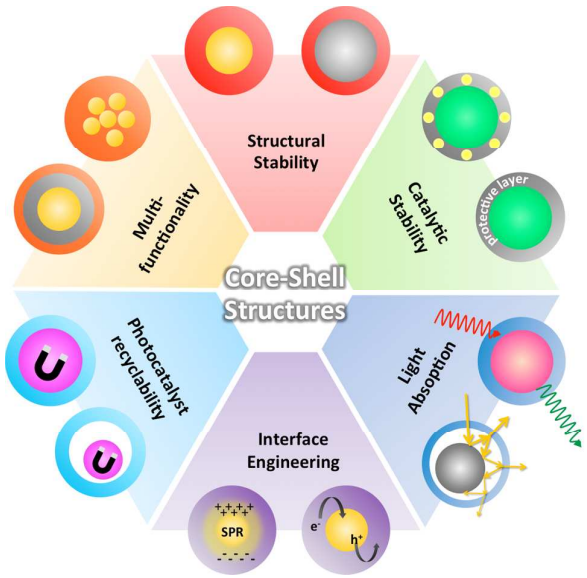

Fig. 3 Schematic diagram of core-shell structured photocatalysts according to their functions.

Among the numerous structural designs, core–shell nanocomposites has attracted considerable attention and developed into an increasingly important research area for photocatalytic applications. Core-shell structures generally feature a chemical composition on the surface that is different from the core, thus exhibiting improved photocatalytic properties as compared to their single-component counterparts. The major functions of the core-shell structure for improving the performance of photocatalysts are shown in Fig. 3. They comprise of i) prevention of undesired migration or dissolution to improve physical structure stability, ii) deterrence of undesirable aggregation or corrosion during photocatalytic reactions, iii) activation of unique optical properties, iv) provision of three-dimensional contact between the shell and the core which maximizes the core–support interaction in terms of charge transfer and localized surface plasmonic effect, v) encapsulation of magnetic materials for recycling, and vi) design of multi-functional photocatalysts.

Depending on the different functions of each material in core-shell photocatalyst, controlled synthesis over shell thickness, porosity and uniformity is important to produce efficient core-shell photocatalysts. The photocatalytic TiO_2 shell is designed with high active surface area, controlled porosity, and optimized thickness for desired purposes. Different morphologies of TiO_2 can be adopted to further improve its surface area, crystallinity, ratio of active facets and accessibility to the reactants. The inner layers of shell can be used as either interactive layer or isolation layer, and sometimes both. In the case of interactive layer, the three-dimensional confinement of the shell allows stronger interaction between different materials for either charge transfer, photon transfer, or energy transfer. When the inner shell is used as isolation layer, it provides perfect insulation to prevent interaction between different materials, or to protect the inner material from photocorrosion and improve stability. The thickness of this layer also needs to be well controlled so that it achieves its desired function, at the same time not diminishing the functionality of other composition. When the inner layer has dual functions, it is critical to control the shell thickness as the coating thickness can be used to tune the properties of the inner core that consists of plasmonic metals, upconversion crystals and magnetic materials. Moreover, various structures beyond simple core-shell configuration, such as yolk-shell, hollow multiple shells, multicore-shell and multicomponent core-shell structures allow many other functions to be incorporated, such as unique optical properties, synergistic effects and recycling of the photocatalysts. Core-shell structures have the flexibility to systematically tune the structures, and thus the functions of the photocatalysts. Through rational design and controlled synthesis of TiO_2 composite core-shell structures with multiple components and well-controlled interactions, they are likely to bring many novel and enhanced benefits to photocatalytic reactions.

3.1 Structural stability

Core-shell structures provide a platform for synthesizing well-controlled structures with high stability. TiO_2 shells can be synthesized on sacrificial template or catalyst materials to form either core–shell (Fig. 4a), hollow (Fig. 4b), yolk–shell (Fig. 4c-d) or double-shell (Fig. 4e-f) structures. Various shapes of cores have also been used, such as nanoparticles (Fig. 4g-h), nanorods (Fig. 4i-l) and nanocubes (Fig. 4m). Moreover, more complex core-shell structures

have also been synthesized, such as multiple-shell structures with (Fig. 4n) and without inner cavity (Fig. 4o-p).

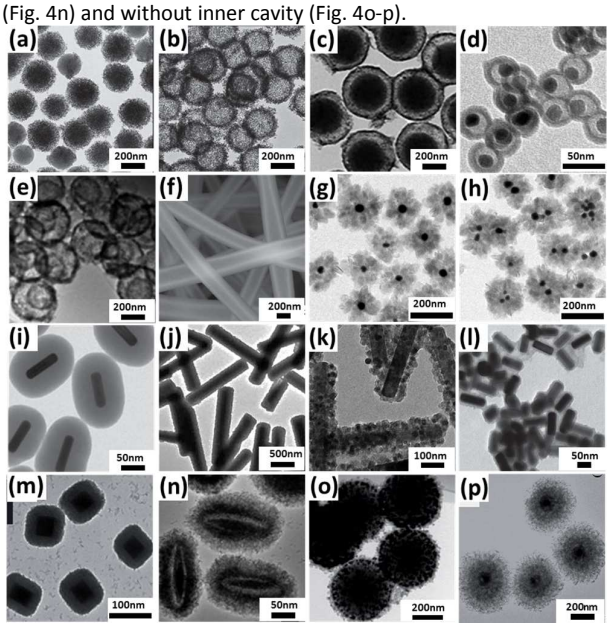

Fig. 4 TEM images of various TiO_2-based core-shell nanostructured photocatalysts. (a) SiO_2@TiO_2 core–shell structures, (b) mesoporous TiO_2 hollow nanostructures, (c) SiO_2@TiO_2 yolk–shell Structures, (d) Fe_3O_4@SiO_2@TiO_2 yolk–shell nanoparticles, (e) double-shell anatase–rutile TiO_2 hollow spheres, (f) Hollow SnO_2/TiO_2 coaxial nanofibers, (g) Au@TiO2 core-shell particles, (h) Au_{multi}@TiO_2 multiple core-shell particles, (i) Gold nanorod@TiO_2 yolk-shell nanostructures, (j) $NaYF_4$:Yb,Tm,Gd microrods@TiO_2 core–shell composite, (k) $NaYF_4$:Yb,Tm,Gd nanorods@TiO_2 core–shell composites, (l) TiO_2 coated Au/Ag nanorods, (m) Cubic Pd@TiO_2 core-shell structures, (n) Ellipsoidal α-Fe_2O_3@TiO_2 yolk-shell structures, (o) SiO_2–Ag–SiO_2–TiO_2 triplex-shell structures, (p) Ag@Fe_3O_4@SiO_2@TiO_2 multiple-shell structures. Adapted from ref. 91, 104-105, 115, 118, 129 and 132-133 with permission. Copyright Royal Society of Chemistry and WILEY-VCH Verlag GmbH & Co. KGaA, Weinheim.

3.1.1 Controlled synthesis Hollow spheres become an intensive area of research for structural design of photocatalysts. The porous shell of TiO_2 hollow structures possess high specific surface area with a large number of active reaction sites, reduced diffusion distance of photogenerated charge carriers, and improved the accessibility to reactants through porous shell. The challenge for developing efficient TiO_2 hollow photocatalysts lies in precise control of its structural properties. There are two synthetic approaches, namely template-free and template-assisted methods. Although template-free method is simple and convenient from a synthetic point of view, they are usually carried out under high temperature and pressure, and it is quite difficult to control the thickness, porosity and crystallinity of the shells.[60] On the other hand, template-assisted methods are more common and universal processes for synthesizing TiO_2 hollow photocatalysts with well-controlled structural properties.[76, 86, 87] The basic process involves preparing a sacrificial template and depositing the nanoscale TiO_2 shell layers to form the core–shell structure, followed by post-crystallization and selective etching to remove the sacrificial template to form hollow TiO_2 shell nanostructures (Fig. 5a). Zhang *et al*[76] and Joo *et al*[72] both synthesized hollow TiO_2 structures based on this process by using carbon nanospheres and SiO_2 colloidal as sacrificial templates respectively. They both demonstrated the crystallinity and phase of hollow TiO_2 spheres with optimized crystallinity that outperform P25 in the photocatalytic dye decomposition. Lu and co-workers[88] reported a method to fabricate mesoporous anatase TiO_2 nanocup crystals through further etching treatment of hollow TiO_2 spheres using NaOH (Fig. 5b). The as-synthesized cup-like anatase TiO_2-based photocatalyst exhibits relatively high conversion efficiency of solar energy to photodegradation compared with hollow TiO_2 spheres and conventional P25 due to its high surface area, mesoporous TiO_2 shell structure, the highly active anatase {101} facet and improved light harvesting ability. Other template-assisted methods have also been developed to produce hollow TiO_2 spheres that aim to provide more controllable way to retain their structures. For example, surface-protected etching method (Fig. 5c) in which an additional silica layer was coated onto the TiO_2 surface to prevent breakage of the shell and inhibit extensive structural changes.[60] Another example is nanoparticle-mediated approach which has high synthetic flexibility for tailoring complex shelled nanostructures with different architectural designs (Fig. 5d).[89] These various forms of hollow structures show the high active surface area, high crystallinity and porous shell that are responsible for improved photocatalytic performance. Core-shell scheme provides a simple method to synthesize these hollow TiO_2 structures with high surface area and well-controlled structural properties that are beneficial for photocatalytic applications.

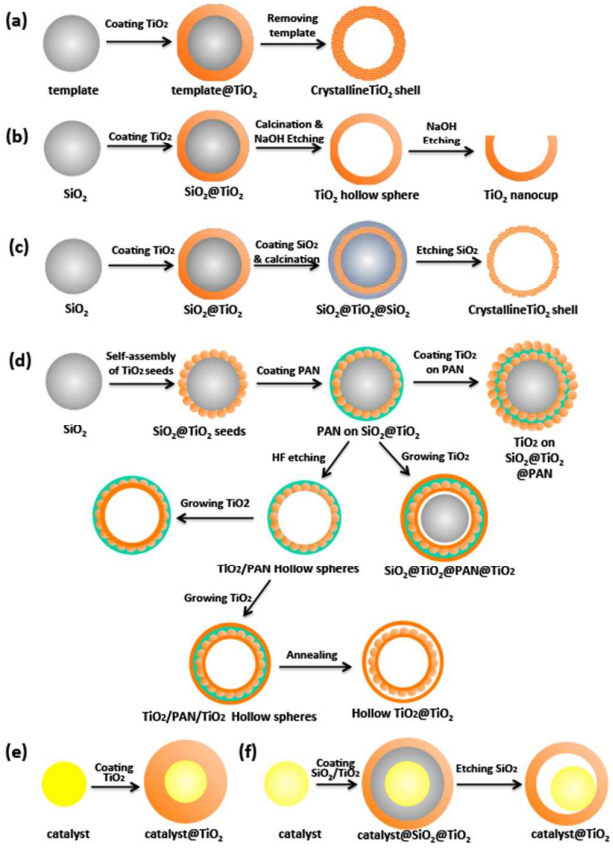

Fig. 5 Different synthesis methods to create hollow TiO_2 structures: (a, b) hollow spheres; (c) nanocups; (d) double-shell hollow spheres; (e) core-shell structure; (f) yolk-shell structure. (PAN: Polyacrylonitrile)

3.1.2 Anti-migration and dislodging of catalysts A typical synthesis of core–shell structures involves coating a layer of TiO_2 onto the catalyst particles (Fig. 5e), while an additional sacrificial intermediate layer is needed for making yolk–shell structures (Fig. 5f). Both core-shell and yolk-shell nanostructures with nanoparticles encapsulated and protected by an outer shell can be used to isolate the catalyst nanoparticles and prevents their migration and dislodging during the photocatalytic reactions. Many groups have demonstrated the advantages of structural stability in these core-shell structures towards improving photocatalytic activities.[60, 90, 91] Our group[91] investigated the photocatalytic stability of three samples (Fig. 6a) of Au on TiO_2 and Au@TiO_2 single (Fig. 4g) and multiple (Fig. 4h) core–shell nanospheres through three cycles of two hours sacrificial water splitting experiment. The Au on TiO_2 shows a decrease of 33% in H_2 evolution due to leaching; whereas the Au@TiO_2 single and multiple core–shell nanospheres exhibit ±5% variation in H_2 evolution (Fig. 6b). Moreover, having a controllable porosity in the TiO_2 shells becomes an extremely important requirement in these cases in order to guarantee the accessibility of the reactant molecules to the encapsulated catalysts. Other works on metal@TiO_2 core-shell photocatalysts have been reported, where metallic nanoparticles including Pt,[16] Pd,[90] Au[91] and Ag[92] have been used to enhance the photocatalytic activity on the TiO_2 surfaces by suppressing the electron-hole recombination. The photo-induced electrons migrate to the metal due to the relatively low Fermi level of metals, which make the photoinduced holes stable on the TiO_2 surfaces by increasing the lifetime of charge carriers. Porous TiO_2 shells are promising structural design, since the porous shells not only prevent the aggregation of core metal nanoparticles but also allow the reactants through the pores to react with inner cores.

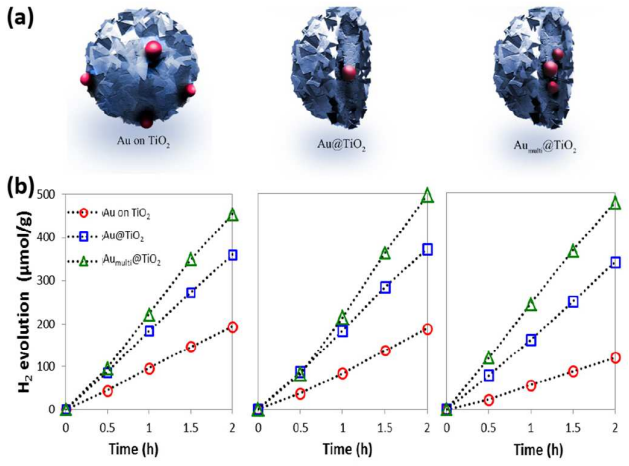

Fig. 6 (a) Schematic of the three different designs of TiO_2 nanospheres synthesized with/without Au nanoparticles, as well as surface loaded or spatially confined Au nanoparticles. (b) Photocatalytic H_2 evolution cycles of Au on TiO_2 and Au@TiO_2 (single and multiple) core–shell nanospheres. Adapted from ref. 91 with permission. Copyright Royal Society of Chemistry.

3.2 Catalytic stability

3.2.1 Active surface area protection One of the major challenges in the use of nanostructured materials as photocatalysts is the stability of the active catalyst particles. As discussed earlier, core-shell or yolk-shell structures offer advantage of structural stability of the catalyst against dislodging and migration. In this section, the catalytic stability of photocatalyst will be discussed. During both the preparation process of photocatalysts and photocatalytic reaction, nanoparticles may rapidly grow larger and sinter into large clusters due to their high surface energy (Fig. 7a). This will result in reduction of the active surface area and loss of photocatalytic activity over time. This is illustrated in Fig. 7b, where well-dispersed Pt nanoparticles of 2-3 nm were seen to sinter into a few large crystalline particles of ~10 to 20 nm after calcination Fig. 7 c.[28,93] Both Ge *et al.*[94] and Zhang *et al.*[95] demonstrated a surface-protected etching method for fabricating core–satellite nanoreactors in which metal nanocatalysts are stabilized by a porous SiO_2 shell, and the procedures involved is shown in Fig. 7d. Metal nanocatalysts are loaded onto SiO_2 colloids surface through electrostatic interactions or chemical bonding. Another SiO_2 layer is coated onto the metal nanoparticles to affix them onto the initial SiO_2 support (Fig. 7e). Finally, the surface-protected etching scheme is applied to transform the outer shell into a mesoporous structure (Fig. 7f), exposing the catalyst particles to outside chemical species. Compared to unprotected metallic nanocatalysts, the as-fabricated structure has consistently shown excellent thermal stability during the catalytic reactions.[95] They have also demonstrated that TiO_2 coated SiO_2/Au core-shell photocatalyst shows high efficiency in catalyzing decomposition of organic compounds under illumination of UV, visible light, and natural sunlight. The structural design of the photocatalyst takes advantage of the synergistic interaction between adsorbed Au and implanted N, and produces stable nonmetal-doped anatase nanoparticles with precisely controlled Au nanoparticles decoration.[96]

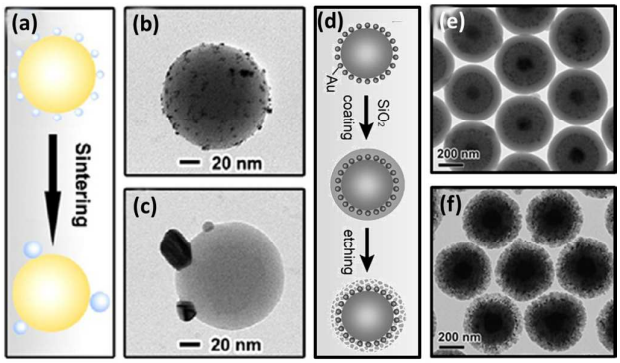

Fig. 7 Illustration of the use of mesoporous silica layers for protection against sintering of dispersed metal nanoparticles. As shown schematically in panel (a), the original small Pt nanoparticles supported on SiO_2 beads (b) coalesce into a few larger structures (c) upon calcination at 1075 K. (d) Schematic illustration of the synthetic procedure used for the formation of SiO_2/Au/SiO_2 sandwiched nanoreactor structures. (e,f) TEM images of the sandwiched structures (e) before, and (f) after surface-protected etching. Note that superparamagnetic Fe_3O_4 particles were included at the core of the samples in (e) and (f) for enhanced recyclability. Adapted from ref. 93 and 95 with permission. Copyright American Chemical Society and WILEY-VCH Verlag GmbH & Co. KGaA, Weinheim.

3.2.2 Corrosion/oxidation inhibition Rational design of core-shell structures can prevent corrosion and oxidation of photocatalyst since the shell can function as a passivation layer. Photocorrosion occurs when the photogenerated holes do not react quickly with

water molecular or organic pollutant, as a result, the holes will react with the photocatalysts which lead to oxidation of the photocatalysts.[97] Many materials suffer from the drawback of having low photocorrosion resistance in most electrolytic media, such as ZnO, CdS, WO_3 and ZnS. This stability issue hinders the use of these materials for long-term photocatalytic applications. Hernandez *et al.*[98] addressed this issue through coating of anatase TiO_2 shell on ZnO nanowires for photocorrosion protection (Fig. 8a). Fig. 8b shows photocorrosion is evidently observed for the ZnO nanowires photoanodes in contrast to a photostable core-shell nanowires photoanodes at a macroscopic level. Moreover, long-term stability photoelectrochemical characteristics of ZnO@TiO_2 core–shell photoanodes for water-splitting are obtained (Fig. 8c). In the case of ZnO, it undergoes photocorrosion through self-oxidation and tends to dissolve in the acidic solution. The photogenerated holes have strong oxidation properties. On one hand, the photogenerated holes can react with water adsorbed on ZnO surface to form highly reactive hydroxyl radicals (OH·) to perform photocatalysis. On the other hand, the holes may also be trapped on ZnO surface and react with surface O^{2-} ion of ZnO to form O_2, leading to the dissolution of ZnO. However with the presence of TiO_2 shell, an efficient channel for the photogenerated holes from ZnO surface to heterosystem/electrolyte boundary is formed. The holes at the boundary preferentially react with water to give the OH radicals to perform photocatalysis. Hence, with the coating of TiO_2, the photocorrosion can be efficiently suppressed and the photostability is significantly improved. Li. and co-workers[99] reported the synthesis of VO_2@TiO_2 core/shell nanoparticles which exhibit enhanced chemical stability of VO_2 against oxidation due to the protective layer of TiO_2. Core-shell nanostructures provide an attractive approach for the protection of catalytic active nanoparticles. There are many possibilities to engineer the core-shell structure in order to protect the chemical stability of the catalysts and at the same time not compromising its photocatalytic activity. The design of porous protective layer is also an important factor to consider for the reactant to reach the active sites of the catalysts.

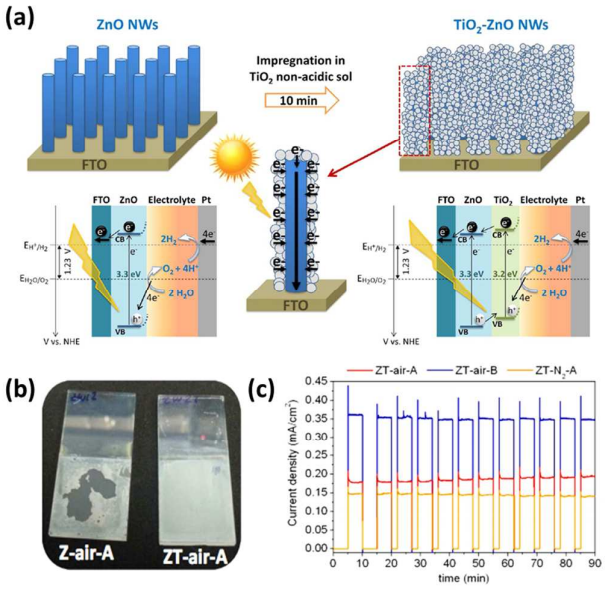

Fig. 8 (a) Scheme of the prepared photoelectrodes, consisting of ZnO nanowires and ZnO@TiO_2 core–shell heterostructures and their band diagrams, which represent the charge carrier transport at the different water-splitting PEC cell interfaces. (b) Picture of the ZnO nanowires (Z-air-A) and the ZnO@TiO_2 core-shell sample (ZT-air-A), treated in air-atmosphere, after the PEC test. (c) Chrono-amperometry measurements (I-t) curves at 0.2V vs. Ag/AgCl (1.2V vs. RHE) over light ON-OFF cycles, of the ZnO@TiO_2 core-shell samples annealed in air (ZT-air-A(one-step annealing) and ZT-air-B(two-steps annealing)) and in N_2 (ZT-N_2-A), under dark and under simulated AM 1.5G solar illumination. Adapted from ref. 98 with permission. Copyright 2014 American Chemical Society.

3.3 Light absorption

3.3.1 Light Scattering In order to improve light absorption, nanostructures that can reflect and scatter light internally are designed. Unlike the nanoparticles which allow the light to pass through (Fig. 9a), core-shell structure formed with materials of different refractive indices allows internal reflection (Fig. 9b),[100, 101] thus improve light absorption capability. Moreover, core-shell structure has been adopted as an intermediate step to create interior cavities within particles which further enhanced scattering and optical localization within the particles.[102] These structures do not only have large surface area, but also allow incident light to undergo multiple light scattering and reflection within the hollow cavities. Such multiple reflection mechanism has been proposed in hollow (Fig. 9c),[103] double-shell hollow (Fig. 9d) [104] and yolk-shell (Fig. 9e)[105,106] structured photocatalysts as illustrated in Fig. 9.

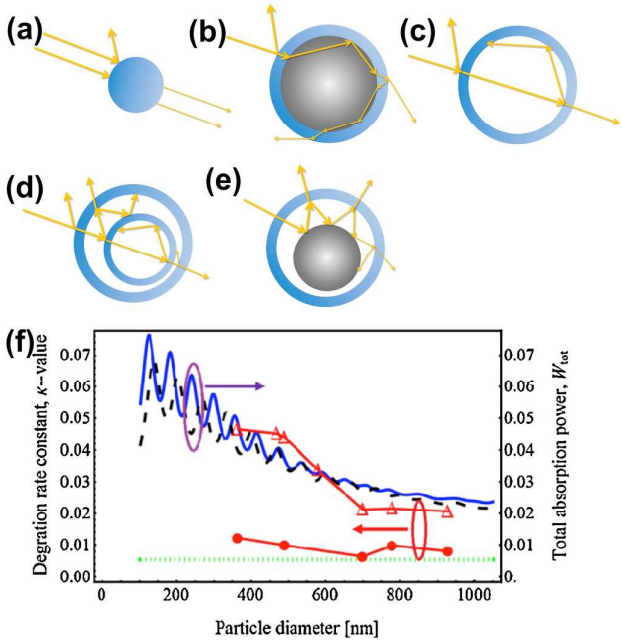

Fig. 9 Schematic diagrams of light pathways in (a) nanoparticles; (b) core-shell spheres (c) hollow spheres; (d) double-shell hollow spheres and (e) yolk-shell spheres. (f) Performance of photocatalytic activities, in terms of the experimental measurement of degradation rate constant-value, for hollow sphere nanoparticles of different diameters (marked by Δ). Numerical simulations of the total absorption power, W_{tot}, are shown for different incident wavelengths: λ= 350 nm (solid-line) and 388 nm (dashed-line), with the thickness of shell in 50 nm. A reference sample, made by crushing the original hollow sphere particles into a powder with the same weight, is shown for the comparison with the experimental data marked by • and its numerical simulations as a dotted-line. Adapted from ref. 109 with permission. Copyright 2013 Elsevier.

In order to design an efficient light absorbing photocatalyst through structural modification, there are a few factors that need to be considered. Firstly, the TiO_2 shell thickness of these nanostructures must be thin enough for the UV light to penetrate through. Unlike nanoparticles which allow light to directly pass through (Fig. 9a), the transmitted UV light through the shell will reflect in the hollow channels. This lead to multiple reflection effects as shown in Fig. 9 b-e, thus enhancing the light harvesting. It has been reported that UV light with intensity of 1 mW cm^{-2} can be completely absorbed by a porous TiO_2 film until its thickness goes beyond several microns.[107] The penetration depth can vary depending on different synthesis methods, particle sizes and porosity of TiO_2 shell. On the other hand, the thickness of hollow TiO_2 spheres ranging from tens to hundreds of nanometers are reported for improved light harvesting.[104, 106, 108] Secondly, the size of the hollow spheres can significantly affect the photocatalytic behavior. Based on the extended Mie's scattering theory, Tsai *et al.*[109] have investigated the light absorption power for hollow TiO_2 spheres with shell thickness of 50 nm, but of different particle diameters (365 to 930 nm) under different incident wavelengths of 350 nm (solid-line) and 388 nm (dashed-line) as shown in Fig. 9f. The numerical results show higher absorption power for hollow spheres of smaller than 500 nm. Thirdly, when multiple hollow channels or yolk-shell structures are designed, the size of the interior cavities and the inner scattering center (inner shell or core) will also affect light scattering. Li *et al.*[106] designed a sphere-in-sphere structure, and showed that with an appropriate inner sphere diameter, the light is used more efficiently, thus offering an improved catalytic activity. Yoo *et al.*[105] also claimed that the yolk–shell structure with a TiO_2 shell and SiO_2 yolk (Fig. 4c) enhances photocatalytic H_2 production, as a result of multiple reflections of UV light within the interior cavities between SiO_2 and TiO_2. The SiO_2 core acts as a scattering center, which also facilitates internal reflections of light (Fig. 9e) and enhances the photocatalytic activity. Lastly, the refractive indicies in different regions due to various materials also affect the scattering, transmitted and internal refracted waves which contribute to total light absorption. Complex hollow structures with multiple shells are highly desirable, as the inner shell can scatter and absorb the light at the same time. Li and co-workers[104] produced a novel double-shell TiO_2 structure (Fig. 4e) with an inner anatase layer and an outer rutile shell using silica protection layer method. The structural effect on photocatalysis was investigated to show higher light absorption than hollow TiO_2, and resulted in enhanced photodegradation.

The structural engineering of interior design of hollow TiO_2 together with optimized size and shell thickness has significant effect on the light absorption power of these hollow spheres, which in turn affect their photocatalytic properties. This multiple light reflection and absorption concept may be generically applied to the design and fabrication of novel nanomaterials with enhanced optical properties for microelectronics, optoelectronics, and other applications.

3.3.2 Upconversion Another way to improve light absorption of photocatalyst is to carry out structural design of core shell structures that encompasses upconversion nanocrystals. The basic mechanism for upconversion materials used in NIR-light active photocatalysis is illustrated in (Fig. 10a). In brief, the NIR light is absorbed by the upconversion nanocrystal itself, which then emits the upconverted UV/visible light. The neighboring UV/visible-active photocatalysts absorb the emitted light from the upconversion nanocrystals to generate electron-hole pairs which can be used to complete the photocatalytic cycle. However, the light conversion efficiency is low because only specific wavelengths of sunlight (800 nm or 980 nm) are used to activate the upconversion crystal. In order to fully utilize the converted light and reduce internal scattering and absorption by upconversion crystal, core-shell structures have been adopted to design efficient NIR-light active photocatalysts. Tang and co-workers[110] designed a core-shell structured $NaYF_4$:Yb,Tm@TiO_2 for NIR-driven photocatalytic degradation and its performance is two times higher compared to the physical mixture of $NaYF_4$:Yb,Tm and TiO_2 sample. This is because the core–shell structured particles allow $NaYF_4$:Yb,Tm and TiO_2 attach closely to each other and form compact interfaces which benefit the photon energy migration process (Fig. 10a) and hence enhance photocatalytic activity. Other researchers also revealed similar results of core-shell structure having superior photocatalytic properties when making efficient use of the converted NIR light for photocatalysis.[111-113] Su *et al.*[114] reported an interconnected porous network of three-dimensional heterostructure consists of upconversion nanoparticles@TiO_2@CdSe core-shell spheres as shown in Fig. 10b. This architecture also provides a close contact between the upconversion particles and photon-absorbing dye that ensures immediate absorption of the emitted light and reduces transmission loss (Fig. 10c). Moreover, the inverse opal structure is known to improve the light-matter interaction due to strong light scattering effect that results in remarkable increase of light path length. The interconnected structure optimally conducts electrons with minimal carrier losses due to its continuous electron conducting pathway (Fig. 10d). By using the as-fabricated three-dimensional core- shell heterostructure, H_2 generation *via* a photoelectrochemical process driven by near-infrared irradiation have been demonstrated. The shell thickness is also a key parameter as it will affect the light intensity for exciting the inner upconversion crystal core, thus the photocatalytic activity. Zhang *et al.*[115] demonstrated highly crystalline TiO_2 shell with different thicknesses can be uniformly coated onto lanthanide-doped $NaYF_4$ microrods (Fig. 4j) and nanorods (Fig. 4k). However, the incident NIR light was attenuated by the shell, which resulted in a decrease in the excitation light intensity arriving at the NaYF4:Yb,Tm core. The results showed that a shell with moderate thickness possesses excellent photocatalytic activity under near-infrared irradiation.

The upconversion materials have shown great promises in extending the optical response of photocatalysts from UV/visible to NIR. However, similar to the previous work, the upconversion efficiency is limited by the narrow excitation bands of upconversion nanoparticles, namely 800 and 980 nm. In view of such limitation, design of upconversion particles with higher efficiency under low light irradiance is needed, and this can be potentially achieved through nanophotonic manipulation with improved photon capturing and confinement abilities to enhance light absorption utilizing a hierarchical core-shell structure.

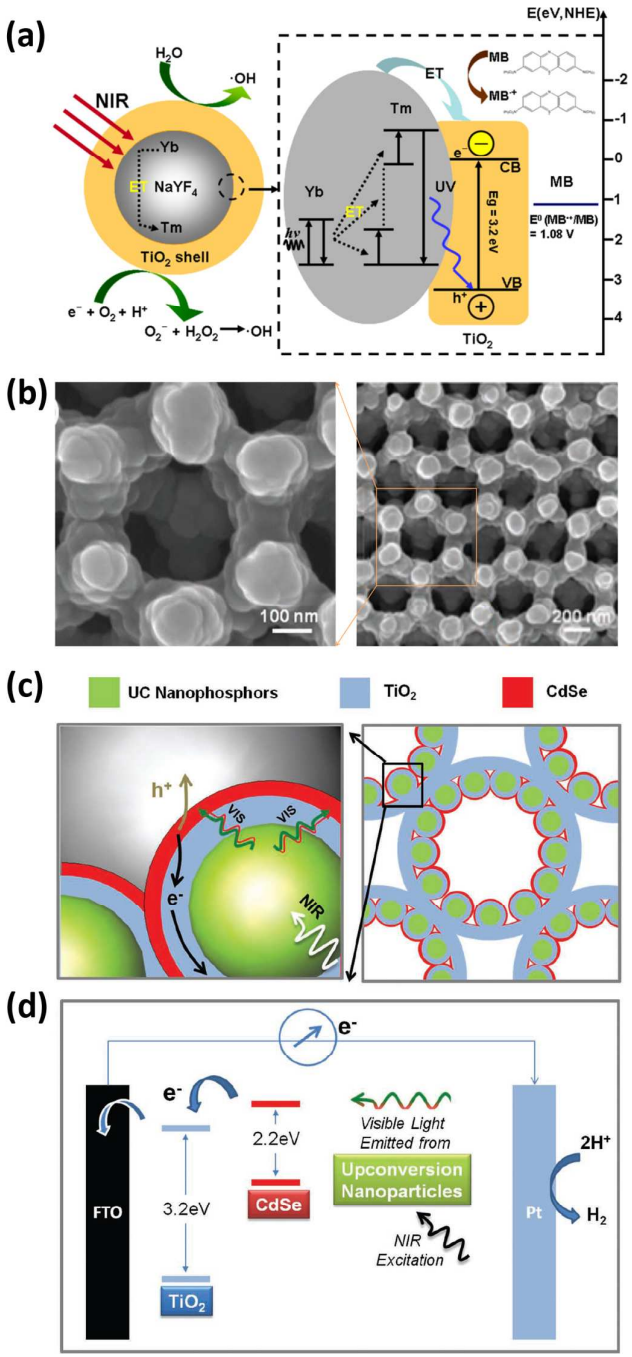

Fig. 10 (a) Schematic diagram of the mechanism of upconversion crystal@TiO_2 core-shell structure. (b) SEM images of TiO_2 deposited on upconversion nanoparticles coupled TiO_2 inverse opals. (c) Schematic of energy flow in the as-prepared hetero-nanostructures from upconversion nanoparticles to visible light-absorbing CdSe nanoparticles to TiO_2 Inverse Opals upon near-infrared photoexcitation. (d) Energy diagram illustrating the charge injection from the excited CdSe into TiO_2 and the transport of photoinjected electrons to the electrode surface for H_2 generation. Adapted from ref. 110 and 114 with permission. Copyright American Chemical Society and Royal Society of Chemistry.

3.4 Interface engineering

Besides enhanced stability, another major advantage that makes core-shell structured catalysts superior than a single component catalyst is the possible synergies derived from interactions between the core and shell materials.

3.4.1 Surface plasmonic effect Noble metal nanoparticles such as Au and Ag have been utilized to enhance the photocatalytic efficiency under visible light. Three primary mechanisms have been discussed according to previous works.[33-35] The first mechanism claims that the enhancement is due to localized surface plasmon resonance (LSPR) effect where hot electrons are generated and transferred to the semiconductor photocatalyst upon visible light irradiation.[14] Another mechanism is based on the plasmon resonance enhanced local electric field of the incident light which causes plasmon resonance energy transfer from metal nanoparticles to TiO_2.[116] The last one is based on efficient scattering mediated by LSPR (far field effect), which leads to longer optical path lengths for photons in TiO_2 that boost the excitation of electron-hole pairs.[117] Zhou *et al.*[118] demonstrated that TiO_2 coated Au/Ag nanorods core-shell structures (Fig. 4l) have improved photocatalytic activity under visible light irradiation, as compared to the mixture of Au/Ag nanorods and P25. This result validates the close contact between the plasmonic metal and TiO_2 in the core–shell structure which allows efficient electron transfer from Au/Ag nanorods to the TiO_2 shell. This prevents direct electron–hole recombination and consequently enhances the photocatalytic efficiency (Fig. 11a). In addition, core-shell structure can also be used to tune the LSPR frequency to the desired range as the surface plasmons of noble metals are very sensitive to the surrounding media. Zhang *et al.*[119] fabricated a well-dispersed triplex Ag@SiO_2@TiO_2 core–shell photocatalyst, which shows a photocurrent density of 38 times larger than that in P25 under visible light due to the plasmonic field of the inner Ag core (Fig. 11b). The SiO_2 interlayer coated on Ag core plays dual vital roles in this case. The LSPR undergoes a blue shift from 497 nm (Ag@TiO_2) to 447 nm (Ag@SiO_2@TiO_2) for a 2 nm SiO_2 shell. As the thickness of the shell increases, the LSPR continues to blue shift which is beneficial for the energy coupling for plasmonic catalysis mechanism as the tuned LSPR wavelength is now closer to the energy bandgap of TiO_2 (Fig. 11c).[119] Not only can the SiO_2 shell tune the LSPR peak to the desired wavelength, it also protects the Ag nanoparticles from oxidation, thus improving the LSPR intensity.[119] This effect has also been observed for Au nanoparticles by Chen and co-workers through both experiments and simulations. Different plasmonic photocatalysts consisting of Au@SiO_2/TiO_2, Au/TiO_2, and TiO_2 were investigated for photodegradation which gave 95%, 80%, and 44% efficiency respectively after 5 h of UV and visible light irradiation. Shell-isolated plasmonic photocatalyst Au@SiO_2/TiO_2 shows the best performance which is verified by the simulation results where SiO_2 coating is seen to significantly increase the LSPR effect of Au nanoparticles (Fig. 11d). The electromagnetic field of Au@SiO_2/TiO_2 improved nearly 9 times compared with Au/TiO_2 (Fig. 11e).[120] In plasmonic core–shell structures, the absorption band is highly dependent on the path length of the shell layer. It is noted that increasing shell thickness may cause a reduction in penetration depth, thus lower the intensity of plasmon resonance. Moreover, the exact position of the plasmon absorption band is sensitive to other factors such as the particle size and shape, and the dielectric constant of the surrounding medium.[121]

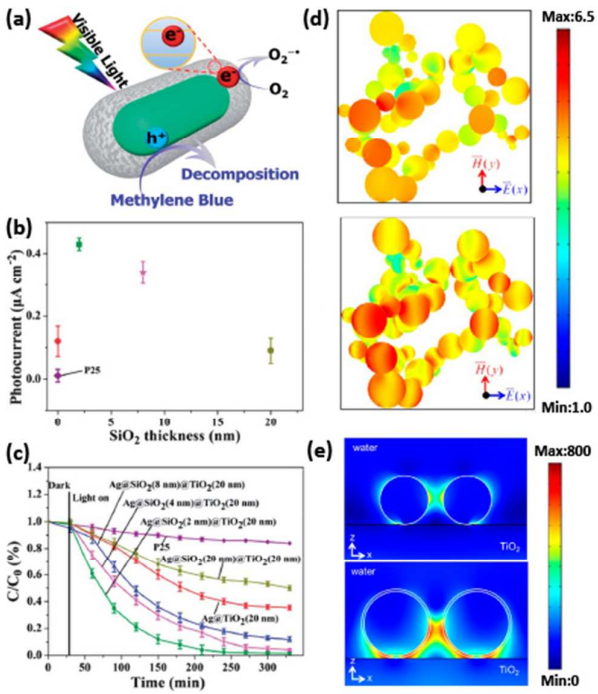

Fig. 11 (a) Schematic representation for the mechanism of photocatalytic degradation of dyes upon visible light excitation. Photocatalytic degradation study of MB, (b) photocurrent study and (c) $\ln(C_0/C)$ versus time line on Ag@SiO_2@TiO_2 (20 nm) with different SiO_2 interlayer thickness.(d) Simulated electric field intensity on the outer surface of Au nanoparticles (up) and Au/SiO_2 core–shell nanoparticles (down) at plasmonic wavelength in logarithmic scale. The wavelength of incident light is 540 nm (up) and 545 nm (down). (e) Simulation of electric field intensity under x-polarized illumination of gold nanoparticles only (up) and gold nanoparticles covered with 3 nm SiO_2 (down) on TiO_2 in the x–z plane (in arbitrary unit). The diameter of nanoparticles is 35 nm (without SiO_2) and 65 nm (with 3 nm SiO_2). Adapted from ref. 118-120 with permission. Copyright American Chemical Society and Royal Society of Chemistry.

3.4.2 Charge separation & transportation As mentioned earlier for plasmonic core-shell photocatalysts, the encapsulation increases the contact area between the two different materials in the core-shell matrix, thus allowing more efficient electron transfer. This spatial confinement has also been used to design composite core-shell photocatalysts for improving charge separation through incorporating either co-catalyst[90, 91, 122-124] or sensitizer[22, 125] into the core-shell matrix. Our group has demonstrated the effectiveness of Au/TiO_2 core-shell structure for interfacial charge-transfer in reducing the recombination of electron–hole pairs in photocatalytic water splitting. We also proved the enhanced and prolonged photocatalytic activity of spatially confined metal cores over conventional surface loaded metal particles, which originates from the structural stability and optimized contact interface for heterojunction-induced charge transfer (Fig. 12a).[91] Zhang *et al.*[125] reported that carbon sensitized TiO_2@C core-shell nanofibers exhibited enhanced photocatalytic degradation efficiency as compared to the pure TiO_2 nanofibers under visible light irradiation. The high separation efficiency of photogenerated electrons and holes is based on the synergistic effect between carbon as a sensitizer and TiO_2 with one dimensional structure (Fig. 12b). Charge separation is one of the key factors that determine the efficiency of photocatalytic reaction. Although photoillumination and transient absorption measurement have been used to study the dynamics of the electron–hole pairs,[91, 126] it is still not very well-understood due to the complexity of many processes that may actually occur at the same time, such as charge carrier generation, electron trapping, inter-band transition, recombination and transportation. Therefore, the use of complementary spectroscopy measurements to understand the dynamics of the electron–hole pairs in core-shell photocatalysts during catalytic reaction is essential for designing efficient photocatalysts.

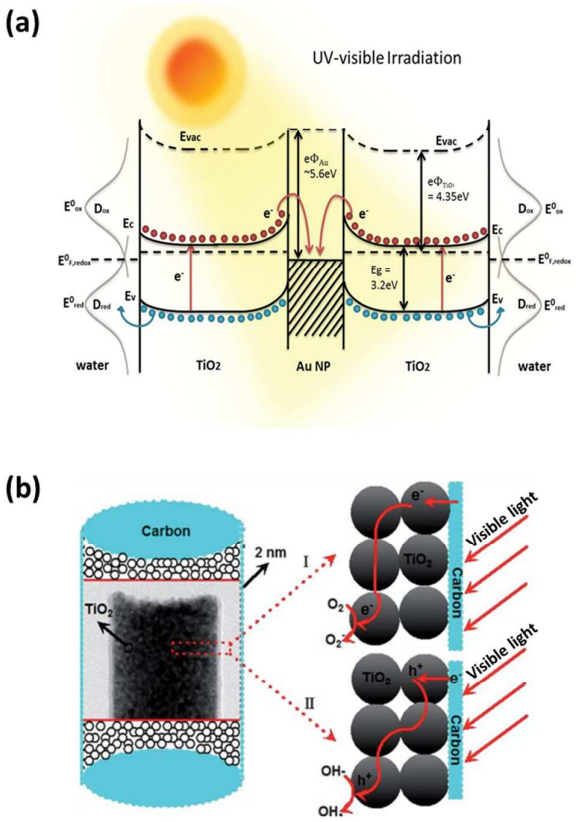

Fig. 12 (a) Proposed photocatalytic mechanism and energy band diagram of the Au@TiO_2 core-shell nanospheres under sunlight irradiation. (b) Visible light-induced photodegradation with the TiO_2@C core-shell nanofibers. Adapted from ref. 91 and 125 with permission. Copyright Royal Society of Chemistry.

3.5 Photocatalyst recycling

Considering that most photocatalytic processes are conducted in solution using suspension form of TiO_2 photocatalysts, separating or collecting these nanosized particles from the solution after photocatalytic reaction becomes difficult. Conventional separation methods, including centrifugation and filtration, may lead to loss of the photocatalysts and an increase in the practical running costs. Thus, it is important to develop a simple way to recycle photocatalysts so that the deactivated photocatalysts can be

recovered and reused in order to reduce excessive use of photocatalysts. Magnetic separation provides a convenient approach for separating and recycling nanoparticles from solution by applying an external magnetic field. This approach is feasible for separating and recovering TiO_2 photocatalysts through integration of magnetic components.[127, 128] Core–shell or yolk shell configuration is favorable in the integrated nanocomposites as TiO_2 shell can protect the magnetic core from dissolution and contamination. Su and co-workers[129] synthesized well-defined yolk-shell Fe_3O_4@TiO_2 nanoparticles (Fig. 13a and Fig. 4d) and its photocatalytic activity was assessed by photodegradation under UV irradiation. These nanoparticles not only exhibit improved photocatalytic performance, but can also be conveniently separated using a magnet and reused. Fig. 13b shows good photocatalytic recyclability and sustainability due to the superparamagnetic behavior of Fe_3O_4 core. Zhang *et al.*[130] demonstrated Ag-coated Fe_3O_4@TiO_2 core-shell microspheres as recyclable photocatalysts that outperform P25 for photodegradation. It is worth noting that the magnetic saturation (Ms) value of the Fe_3O_4 (77.5 emu g^{-1}) microspheres is significantly higher than that of the Fe_3O_4@TiO_2 microspheres (38.7 emu g^{-1}) and Ag-coated Fe_3O_4@TiO_2 microspheres (36.8 emu g^{-1}) as shown in Fig. 13c. Moreover, it can be seen that there are no significant changes in the coercivity (Fig. 13d). Such excellent magnetic properties imply strong magnetic responsivity of the core-shell structure, which enables them to be separated easily from solution with applied external magnetic force (Fig. 13e). These core-shell photocatalyst recycled by the external magnetic field facilitates easy reuse and regeneration of photocatalysts. Other materials structures that can be fabricated for easy recycling include thin films and hydrogel matrix. However, the reactivities of such photocatalysts are considerably reduced since the effective surface area and light absorption are significantly decreased. Although some effort have been made in designing and fabricating magnetic core-shell structures as convenient and recyclable photocatalysts, the stability of such photocatalysts must be further improved.[131]

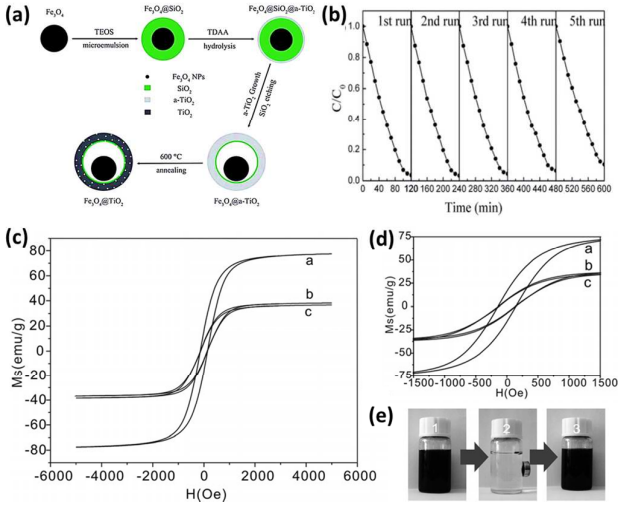

Fig. 13 (a) Schematic illustration of the synthetic strategy to produce Fe_3O_4@TiO_2 yolk–shell nanostructures. (a-TiO_2 denotes amorphous TiO_2). (b) Recyclability of the Fe_3O_4@TiO_2 nanoparticles for the degradation of RhB solution via magnetic separation. (c) Magnetic hysteresis loops and (d) the enlarged view of the central loops of a) Fe_3O_4 microspheres, b) Fe_3O_4@TiO_2 microspheres, and c) Ag-coated Fe_3O_4@TiO_2 microspheres. (e) Photographs of 1) a 1×10^{-5} M methylene blue (MB) solution after UV irradiation for ca. 35 min with dispersed Ag-coated Fe_3O_4@TiO_2 microspheres, 2) the solution after magnetic separation using an external magnetic field, and 3) the 1×10^{-5} M MB aqueous solution with redispersed Ag-coated Fe_3O_4@TiO_2 microspheres after shaking. Adapted from ref. 129 and 130 with permission. Copyright Royal Society of Chemistry and WILEY-VCH Verlag GmbH & Co. KGaA, Weinheim.

3.6 Multi-functional core-shell photocatalysts

The synergetic effects of multiple semiconductor photocatalysts have been extensively exploited for photocatalytic applications. Core-shell design, whereby each shell layer can be defined within a regulated scale to introduce a specific feature and with the multiple core-shell structural engineering, a range of unique characteristics associated to physical and chemical stability, light absorption, electron and hole separation and transport and recyclability can be realized.[131]

Core-shell design provides a platform for incorporating different materials with isolated functions into one integral design. By coating an inert layer which separates the two different materials, each individual material can function independently without undesired interference with each other. Zhou and co-workers[132] designed and synthesized SiO_2–Ag–SiO_2–TiO_2 multi-shell photocatalysts (Fig. 14a and Fig. 4o) with wide-spectral-response. The photocatalytic activity tests showed enhanced photocatalytic efficiency under both UV and visible light irradiation. The main reasons for the enhancement of the photocatalytic activity are (Fig. 14b) (1) the dense Ag nanoparticles covering the SiO_2 core form many “hot spots” and induce a stronger excited localized surface electromagnetic field. (2) The N-doped anatase TiO_2 enhances light absorption in the visible light region. (3) The silica interlayers between Ag and TiO_2 shell prevent electron transfer and increase the stability of Ag. (4) The precise thickness control of the SiO_2 interlayers that tunes the distance between Ag and TiO_2 layers is beneficial to adjust the coupling between the LSPR of Ag nanoparticles and the TiO_2.

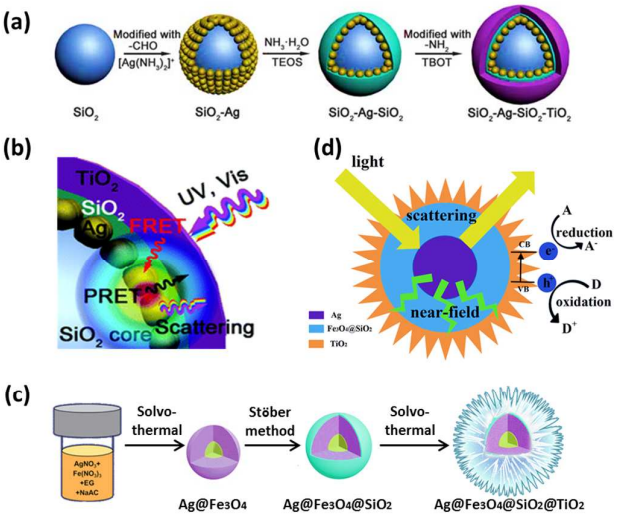

Fig. 14 (a) Synthesis process of the SiO_2–Ag–SiO_2–TiO_2 multi-shell structure. (b) Mechanism of the photocatalytic processes of SiO_2–Ag–SiO_2–TiO_2 sample. (c) Schematic illustration of the fabrication of Ag@Fe_3O_4@SiO_2@TiO_2 nanospheres. (d) Mechanism of the photocatalytic processes of Ag@Fe_3O_4@SiO_2@TiO_2 sample. Adapted from ref. 132 and 133 with permission. Copyright Royal Society of Chemistry.

Moreover, multiple functions can be integrated into one single design through core-shell structure. Su *et al.*[133] demonstrated the design and fabrication of the well-defined triple-shelled $Ag@Fe_3O_4@SiO_2@TiO_2$ nanospheres with burr-shaped hierarchical structures (Fig. 14c and Fig. 4p), in which the multiple distinct functional components are integrated into this single nanostructure (Fig. 14d). The Ag core is used to extend the photo-response of TiO_2 to the visible region through inducing electromagnetic field magnification and efficient resonance photon scattering. The compact Fe_3O_4 shell facilitates the modulation of LSPR of Ag nanoparticles and provides efficient magnetic separation. The SiO_2 interlayer protects Ag and Fe_3O_4 from corrosion and oxidation, which improves the stability of the catalyst. This SiO_2 interlayer between the Fe_3O_4 nanoparticles and TiO_2 hierarchical structure also inhibit the direct transfer of electrons–holes from TiO_2 to the Fe_3O_4 layer, which favorably prevents pronounced Fabry–Perot oscillations. Finally, the outermost TiO_2 hierarchical shell assembled by super-thin nanosheets with high surface area is beneficial to promote the adsorption of pollutants, allowing more effective transport of the reactant molecules or ions to the active sites. In comparison with P25, the triple-shelled $Ag@Fe_3O_4@SiO_2@TiO_2$ nanospheres exhibit outstanding adsorption and degradation of pollutant under visible light or natural sunlight irradiation.

4. Hierarchical structures of TiO_2

Single constituent or basic nanostructures of TiO_2 are known to exhibit photocatalytic properties for energy and environmental applications. However single constituent TiO_2 nanostructures are generally lack of befitting properties and tend to aggregate during material processing and photocatalytic reaction, hence limit their photocatalytic performance. One strategy to overcome the aforementioned limitations is to engineer TiO_2 into hierarchical nanostructured materials. A hierarchical nanostructured material is defined here as a higher dimension of a micro- or nanostructure composed of numerous low-dimensional basic structures. In essence, it consists of nanosized entities that integrate various nanoscale building blocks of dissimilar dimensionality, morphologies and compositions etc. Rather than just geometrical assembly consideration to prevent aggregation, combination of disparate entities can potentially improve or multiply the functional characteristics of a single constituent material. Furthermore, the accomplishment of hierarchical nanostructured materials represents a valuable means of materials manipulation at an unprecedented length scale, to enable probing of specific structure to elucidate structural influence on photocatalytic properties.

Hierarchical TiO_2 composite material is a hot topic in recent years and diverse hierarchical structures have been designed and applied to photocatalysis. The design of TiO_2 hierarchical structures commonly involves growth of nanoscale building blocks on the inner and/or outer surfaces of host materials. These building blocks can be zero-dimensional nanoparticles,[134] one-dimensional nanostructures such as nanorods,[135] nanowires,[136] nanotubes[137] etc. and two-dimensional such as nanosheets,[138] nanoflakes[139]. The composition of secondary structures can be similar or different from the host matrix to form hierarchical assembly of homogeneous or heterogeneous composite structures, respectively. The hierarchical designing concept makes it possible to engineer the function of TiO_2 composite materials in which not only the excellent properties of the host matrix are preserved, but also to introduce additional function of secondary structures, such as enhanced surface area, improved solar absorption and utilization, fast electron transport and efficient charge collection, and so on, are integrated, forming multi-functional materials. In light of all these functional attributes, we have focused on the designing and engineering of hierarchical TiO_2 materials for advanced photocatalysis applications where key factors such as specific surface area, light harvesting ability, exposed facet, mixed phase and heterojunction will be discussed (Fig. 15).

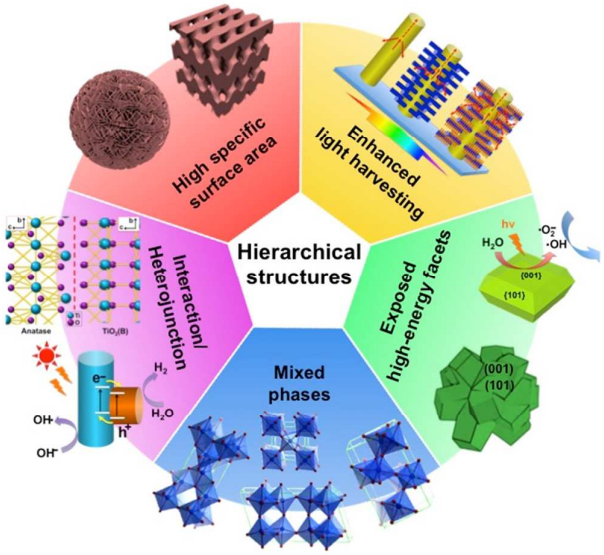

Fig. 15 Schematic diagram of hierarchical structured photocatalysts according to their functions.

4.1 High specific surface area

It is known that photocatalysis takes place at a material surface hence the accessibility to reactants must be high. Surface accessibility is directly related to the porosity of a material. A high specific surface area increases exposure of active sites and solid-liquid interfaces for photocatalytic reaction. It is noted that effort to enhance photocatalysis by increasing surface area through the decrease of particle sizes down to several nanometer is often setback by the attractive Van der Waals forces that lead to large agglomerates. As a result, the diffusion of reactant into the interior of the large aggregates is ineffective due to small pores, long diffusion length, and tortuous pathways. A promising way to overcome the limitation is to compose hierarchical structure that consists of non-agglomerated entities that do not compromise its surface area. In contrast to the agglomerated structures, hierarchical nanostructured materials can be assembled either in irregular fashion with variable pore size distribution or in periodic fashion with uniform pore-size distribution.With highly organized structure, the accessibility to reactant molecules, the rate of mass transfer for reactant adsorption as well as other attributes (to be discussed later) can be significantly improved.

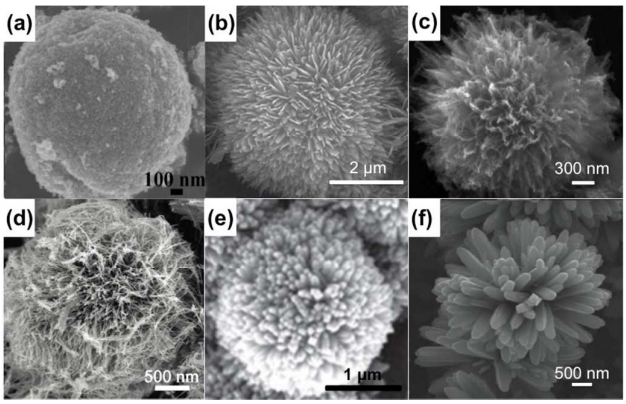

Fig. 16 SEM images of various TiO_2-based hierarchical nanostructured photocatalysts with different building units (a) Particles, (b) Nanosheets, (c) Nanoflakes, (d) Nanowires, (e) Nanothorns and (f) Nanorods. Adapted from ref. 104, 134-136 and 138-139 with permission. Copyright Royal Society of Chemistry, Elsevier and American Chemical Society.

In the recent years, hierarchical TiO_2 catalysts with interesting morphologies and of high specific surface area have been designed and fabricated for photocatalysis applications, ranging from hierarchical spheres to mesoporous film matrix. For the case of hierarchical TiO_2 spheres, various building blocks ranging from zero-dimensional, one-dimensional to two-dimensional nanostructures have successfully been assembled and applied to photocatalysis (Fig. 16). Ming *et al.*[140] have prepared hierarchical TiO_2 spheres that are made up of zero-dimensional nanoparticles. The obtained hierarchical TiO_2 spheres possess high specific surface area (234 $m^2 g^{-1}$), large pore volume (0.36 $cm^3 g^{-1}$), and uniform pore size (11 nm) distribution. Similar hierarchical spheres consisting of zero-dimensional nanoparticles of high surface area of 277 $m^2 g^{-1}$ were fabricated.[141, 142] Both structures show excellent organic and inorganic pollutant degradation under UV and visible light irradiation. An added advantage of using such hierarchical TiO_2 sphere for photocatalysis is the ability to separate and recycle them by simple filtration process due to their overall large particle size. This is verified by repeated photocatalysis reaction that displayed stable and nearly constant photo-decomposition rate. On the other hand, Bai and co-workers[143] have synthesized hierarchical TiO_2 spheres that are made up of one-dimensional nanowire and nanoribbon. The specific surface area is ~100 $m^2 g^{-1}$, relatively higher than that of P25 (34 $m^2 g^{-1}$). The hierarchical structures show not only enhanced photodegradation of organic pollutants but also high permeation flux owing to high surface area and fairly dense packing of one-dimensional nanostructures which poses less resistance to water penetration as compared to compact nanoparticles. Other design of hierarchical TiO_2 spheres that are made up of two-dimensional nanosheet building blocks have also been synthesized for photocatalysis application. These high surface area (~170 to 400 $m^2 g^{-1}$) hierarchical spheres with flower-like morphology were assembled from nanosheets or nanoflakes. Similarly, the hierarchical TiO_2 photocatalysts show excellent adsorption ability and high photodegradation rate.[144, 145]

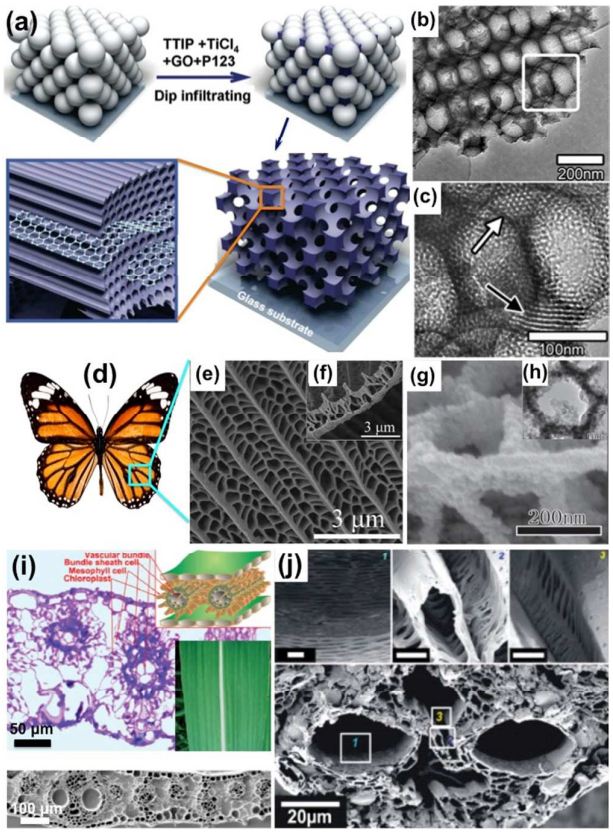

Fig. 17 (a) Illustration for the preparation of macro–mesoporous TiO_2–graphene composite film. (b-c) TEM images of macro–mesoporous titania films. (d) Photograph of the entire wings. (e-g) SEM and (h) TEM image of butterfly wing architecture TiO_2. (i) Cross section of a Saccharum officinarum Linn. leaf observed using an optical microscope; the inset shows an illustration of the Kranz–type anatomy and digital picture of leaf. j) Cross–sectional SEM image of leaf morph–TiO_2; the inset shows a magnification of the corresponding areas contained the white panes: the scale bars are 2 mm. Adapted from ref. 149-152 with permission. Copyright Royal Society of Chemistry, Elsevier, American Chemical Society and WILEY-VCH Verlag GmbH & Co. KGaA, Weinheim.

Another type of high surface area TiO_2 hierarchical structure that is of great interest is the mesoporous material. Mesoporous materials have many fascinating properties such as tunable pore sizes, high surface areas, large pore volumes, variable pore shapes, and controllable framework compositions. TiO_2 mesoporous structures of well-defined pores endow large surface-to-volume ratios and efficient diffusion pathways for guest species, such as water and organic pollutants, to support efficient photocatalysis. In general, ordered mesoporous TiO_2 can be synthesized using soft or hard templates.[146] More commonly, soft template based on sol–gel methods using a variety of surfactants and block co-polymers have been employed to synthesize tailored TiO_2 hierarchical structure. The hierarchical structures composed of zero-dimensional nanoparticles showed enhanced adsorption capacity, water permeability and photocatalytic performances.[147-149] Du *et al.*[149] have employed a confinement self-assembly method to create regular voids of a three-dimensional periodic colloidal crystal, using Pluronic P123 and polystyrene spheres as a mesostructured template and a macro-structure scaffold, respectively (Fig. 17a). Macro-mesoporous titania films possess a well-ordered two-

dimensional hexagonal (p6mm) mesostructure and well-interconnected periodic macropores as well as high specific surface area (299 $m^2 g^{-1}$) and large pore volume of (0.57 $cm^3 g^{-1}$), (Fig. 17b-c). Incorporation of interconnected macropores in mesoporous films significantly improves the mass transport through the film, reduces the length of the mesopore channel, and enhances the accessible surface area throughout the matrix. The unique macro to mesoporous structures showed enhanced capacity of rapid adsorption and photodegradation of organic dyes.

Other method of synthesizing exquisite hierarchical structures can be offered by Mother Nature and borrowed as bio-templates. Bio-templates such as butterfly wing and leaf architectures have been used for synthesizing TiO_2 replicas.[150-152] These templates show complex morphology consisting of lamellas and columns, which are in turn arranged into highly ordered architectures forming pores. Based on the prototype of the hierarchical architecture of butterfly wing (Fig. 17d-h) and leaf (Fig. 17i-j), mimic TiO_2 hierarchical structures were produced by a simple immersion/infiltration-calcination method. The bio-templated TiO_2 hierarchical structures have demonstrated high surface area and enhanced photocatalytic properties.

Hence, the design of TiO_2 hierarchical structure needs to take into the account of porous structure formation not only at the surface but also throughout the bulk of the materials to ensure high specific surface area and pore volume material. With the presence of pores, preferably open, homogenous, ordered and interconnected pores network, physical and chemical properties, as well as extended reactant adsorption and interaction will greatly enhance the photocatalysis reactivity.

4.2 Enhanced light harvesting

Photocatalysis is initiated by light absorption as such it is initially restricted by the number and energy of photons harvested and absorbed by the photocatalyst. One approach to increase the number of photons harvested is to trap light inside a photocatalyst by using wavelength-scale textured nanostructures that minimize reflection losses at the front surface as well as structures that are designed to trap the light within the photocatalyst. Well-designed hierarchical structure strongly favors efficient harvesting of light. When the hierarchical structure is designed to have regularly assembled architecture, a series of optimized processes from multiple light scattering and absorption within the porous structure to light propagation in the presence of periodic columnar structure acting as light guides can be activated. It is noted that multiple light scattering and increase in optical path length can also be attained with less regularly arranged hierarchical structures.

Spherical hierarchical structures that are designed to be hollow and partially open favors light collection and multiple light scattering to improve photocatalytic activity. Liu *et al.*[153] reported such TiO_2 hierarchical structures shaped like bowls, ink-bottles, and rings. These hierarchical structures consist of small nanoparticles or polygons diameter of *ca.* 10-20 nm that are tightly packed to form mesoporous structures. Furthermore, diameter of spherical hierarchical structures has been reported to affect photocatalysis performance. Yang and co-workers[154] have fabricated and optimized hierarchical TiO_2 microspheres with diameters ranging from 0.5 to 10 μm (Fig. 18a-b). The enhanced photodegradation of the microscale inverse opal spheres made up of hexagonally ordered pores was attributed to the synergetic effect of the Mie scattering (Fig. 18c). The angular scattering showed favorable decrease in forward light scattering and increase in side angles scattering with smaller TiO_2 hierarchical spheres. Nonetheless, the particle should not be too small as such it compromises the light scattering intensity. Other than the spherical hierarchical structures that are designed to be hollow and partially open, Tsai *et al.*[155] have synthesized hollow hierarchical TiO_2 cube consisting of anatase nanoparticles (Fig. 18d). Cube shaped NaF salt was adopted as the template where TiO_2 preferentially grew on the edges and corners of the cube to form open cube framework (Fig. 18d insets). These hierarchical structures with nano-sized anatase particles and micro scaled cage architecture markedly enhance the light harvesting by multiple-light scattering, resulting in improved photodegradation of organic compound.

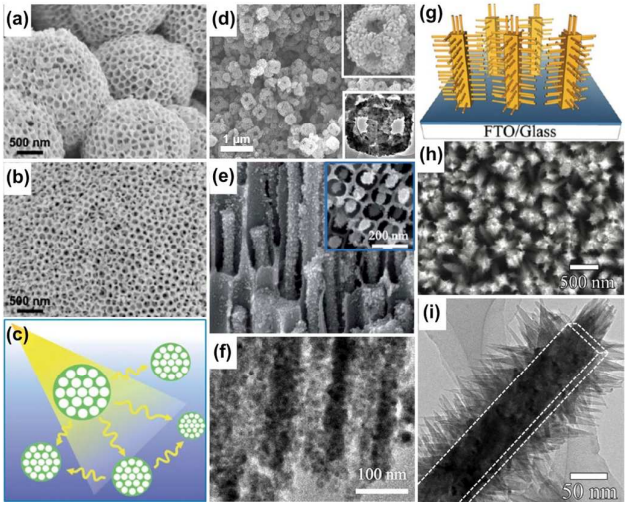

Fig. 18 (a-b) SEM images of hierarchical inverse opal TiO_2 photonic crystal spheres. (c) Light scattering schematic diagram of as-prepared TiO_2 spheres. (d) SEM and TEM images of porous cubic TiO_2 cages. (e-f) SEM and TEM images of the anodic TiO_2 nanotubes. (g) Schematic description and (h) corresponding SEM images of branched nanorods. (i) TEM image of a single nanorod. Adapted from ref. 154-158 with permission. Copyright Royal Society of Chemistry, Elsevier and American Chemical Society.

The important role of meso-macroporous hierarchical structure has been discussed earlier for high surface area. In fact, periodic assembly of bimodal meso-macroporous TiO_2 also contributes to beneficial light absorption and scattering within such hierarchical porous system. The existence of macrochannels can increase photoabsorption efficiency and allow efficient diffusion of reactant molecules. In essence, the microchannel can act as a light transfer path for directing incident photon flux into the inner surface of mesoporous TiO_2. This efficient light harvester configuration allows light waves to penetrate deep inside the bulk photocatalyst. Chen *et al.*[156] have fabricated hierarchical meso-macroporous TiO_2 nanostructures with wire-in-tube architectures *via* anodization and hydrothermal methods (Fig. 18e). The hierarchical wire-in-tube structure is composed of TiO_2 nanoparticles with diameter around 10 nm (Fig. 18f). The periodic wire-in-tube microchannels tube

structure exhibited better absorption attributed to light illumination and scattering throughout the bulk of the hierarchical structure.

In the case of one-dimensional hierarchical structures, branched TiO_2 nanorod structures have been synthesized as efficient photoelectrochemical anodes Fig. 18g-i).[157, 158] The hierarchical structure offers increased light absorption path length due to enhanced light scattering between the branched nanorods. The incident photon-to-current conversion efficiency reaches 67% at 380 nm with an applied bias of 0.6 V versus RHE, nearly two times higher than the bare nanorods without branches.[158] Furthermore, one-dimensional nanostructures offer additional benefit of augmented charge transport and reduced electron–hole pairs recombination by providing a direct conduction pathway for the photogenerated electrons.

Other than the large surface area rendered by the bio-templates as discussed previously, butterfly exhibits brilliant colors due to their wonderful skills of light manipulation, originating intrinsically from their elaborate architectures. The delicate architectures of butterfly compound eyes and wings are primarily based on nipple arrays, regular network and photonic crystal structures, all of which demonstrate the exquisite physical manipulation of light. The bio-templates structures derived *via* simple immersion–calcination method can broaden the horizon of designing efficient light harvesting photocatalyst. For instance, the inverse V-type ridges dominant in black wing scales of butterfly *Ornithoptera Goliath* display antireflection and angle regulation of incident light. Furthermore, the TiO_2 photocatalyst applying black butterfly wings as templates displayed 30% light absorption enhancement and shifting of light absorption to shorter wavelength to complement TiO_2 bandgap. The polycrystalline structures with different oriented gyroid subdomains in some butterflies exhibit omnidirectional colors with different spectral properties. With appropriate lattice parameters, filling fractions and refractive indices, the gyroid domains can obtain omnidirectional light within particular frequencies around the band gap of photocatalyst. This introduces more photons interaction with the photocatalyst and favourably improves catalytic efficiency. [159]

Hence, it is rational to design hierarchical structured materials composed of nano/meso to macro scale structure that can reinforce the light harvesting efficiency through strong light scattering effect, while the nanobuilding blocks including zero-dimensional nanoparticles, one-dimensional nanorods, nanowires etc., that can effectively improve the surface area and simultaneously enhance the light scattering ability within the subdomains of the hierarchical structure.

4.3 Exposed high-energy facets

The average surface energies of anatase TiO_2 have been calculated to be 0.90 J m^{-2} for {001}, 0.53 J m^{-2} for {100} and 0.44 J m^{-2} for {101}.[160] Based on the Wulff construction, surface energy minimization is the driving force towards optimal formation of a crystal shape and facet. Unfortunately, majority of the external surface (more than 94%) of a thermodynamically stable shape anatase crystallites consists of less reactive {101} facets. On the contrary, the {001} facet known for its high photoreactivity characteristics, has low stability meaning that the {001} facet will diminish quickly during the crystal growth stage, resulting in crystal that is dominated by the less reactive {101} facet. The origin of the high reactivity properties of {001} have been attributed to high density of surface undercoordinated Ti atoms and, probably more importantly, the strained configuration of the surface atoms. In particular, the existence of large Ti–O–Ti bond angles suggests unstable and highly reactive 2*p* states oxygen atoms. Evidently, the {001} high-energy facet has shown higher quantum efficiency of surface-mediated photocatalytic redox reactions due to the favorable dissociative adsorption of water and reactant molecules and separation of photoexcited hole/electrons.[161] Hence, the preparation of TiO_2 hierarchical structure that is largely made up of reactive facet {001} is pursued in anticipation of high photocatalytic performance.

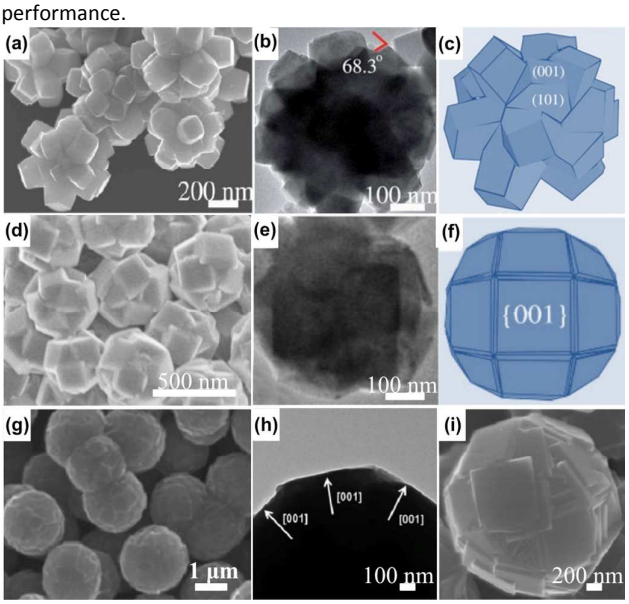

Fig. 19 (a, d, g and i) SEM and (b, e and h) TEM images of the TiO2 nanospheres with dominant exposed {001} facets. (c and f) the corresponding FFT patterns. Adapted from ref. 164-166 with permission. Copyright Royal Society of Chemistry and WILEY-VCH Verlag GmbH & Co. KGaA, Weinheim.

The synthesis of various nanobuilding blocks with exposed {001} facets and their self-assembly into hierarchical architectures have garnered a lot of interest since it is noted that P25 possesses only < 5% of exposed {001} facets.[162] It was found that {001} facets of anatase TiO_2 with five-coordinate Ti atoms are tunable by controlling the surface adsorbates. Accordingly, additive/capping agents that selectively bind to specific crystalline facets are chosen as an effective approach to control the crystal shape. The adsorbed species change the relative stability of the different crystal facets, or inhibit the crystal growth in high index facet, thus altering the equilibrium shapes of anatase TiO_2, resulting in a shape that, ideally controlled by the nature and concentration of the additives. Through experiments and first principle calculations, it has been established that F-terminated surfaces of anatase TiO_2 are largely dominated by {001} facets. [66, 163]

Hydrothermal method is frequently used to prepare spherical hierarchical TiO_2 structure with exposed {001} facets since the addition of hydrofluoric acid aqueous solution to induce fluoride-mediated crystal growth can be conveniently implemented. Here, Liu *et al.*[164] reported the preparation of spherical hierarchical TiO_2

nanostructures that are composed of large numbers of truncated tetragonal pyramidal TiO_2 nanocrystals (*ca.* 100–200 nm) that expose {001} and {101} facets (Fig. 19a-c). By calculations, it is derived that these F-terminated TiO_2 nanostructures contain about 10–30 % of highly reactive {001} facets. Owing to their chemically active {001} facets, these TiO_2 nanostructures exhibited enhanced photocatalytic efficiency. Beside this work, Li *et al.*[165] also synthesized similar spherical TiO_2 made up of truncated tetragonal-pyramidal nanocrystals however with much higher percentage of exposed {001} facets of ~ 78% (Fig. 19d-f). The top square surfaces and four isosceles trapezoidal surfaces consist of {001} and {101} facets, respectively. Here, the influences of the reaction temperature, amount of hydrofluoric acid, and reaction time were optimized for increase {001} facets exposure. Consequently, the TiO_2 nanospheres exhibited greatly enhanced photocatalytic organic degradation efficiency. In order to further increase the percentage of exposed {001} facet of a spherical hierarchical structure, efforts to synthesize structure that are composed of two-dimensional interconnected nanoflakes have been demonstrated (Fig. 19g-i).[166] The individual square nanoflake is connected closely with its neighbors, resulting in the complete exposure and surface coverage of the high energy {001} facets up to 90%. The as-prepared spherical hierarchical structure using hydrofluoric acid generated in situ through hydrolysis of titanium tetrafluoride (TiF_4) as a capping and stabilizing agent. Such large exposure of reactive {001} facets crystal and with F atoms termination structures, show excellent photodegradation of toxic organic contaminants as well as photocatalytic production of H_2 under UV light irradiation.

Aside, less attempts have been made towards creating TiO_2 spherical hierarchical structure that is hollow, high surface area and has exposed {001} facets. Liu and co-workers[162] reported hollow hierarchical structure that consists of small TiO_2 polyhedra, typically truncated bipyramids or decahedra, having sizes between 50 and 100 nm (Fig. 20a-c). With the adsorption of active F ions and the dissolution of the interior space, hollow hierarchical structure of *ca.* 20% exposed {001} facets is formed. Selective adsorption and photocatalytic decomposition of dye molecules were accomplished by using the TiO_2 spherical hierarchical with exposed {001} facets and tailored surface chemistry.

In previous work, nanocrystals dominated with exposed {001} facets are used as the building block for TiO_2 hierarchical structures which still impose some limitations in the specific surface area. Fang *et al.*[167] reported a solvothermal process for synthesizing flowerlike three dimensional hierarchical structures (Fig. 20d). The hierarchical structure is predominantly made up of 97% single-crystalline anatase TiO_2 nanosheets of {001} facet with thickness of around 10–20 nm. The two-dimensinal anatase TiO_2 nanosheets is unique since it only contains few tens of layers of crystal units along the [001] crystallographic direction.

Most of the mentioned work is based on powdered hierarchical TiO_2 nanosheets or granular supported nanosheets, which are difficult to recycle from aqueous solution after photocatalytic reactions and will cause secondary pollution. To solve this problem, an ideal way is to grow these monodispersed nanosheets on carbon fibers support (Fig. 20e). Compared to the traditional stiff substrate, carbon fibers are flexible, conductive, and stable in corrosive conditions, and they enable radially growth around each individual fiber without agglomeration thus resulting in a high exposure area and large surface area, which is critical for photocatalysis applications. Guo and co-workers[71] have reported such synthetic strategy of high-reactive facet dominated TiO_2 hierarchical structures (Fig. 20f-h). The carbon fibers are uniformly and compactly covered by a large number of tetragonal nanosheets with a thickness of 40–65 nm and side length of 500–800 nm. The percentage of {001} facets in TiO_2 nanosheets was calculated to be 40-92%, depending on the concentration of fluorine ions. The TiO_2 nanosheet on carbon fiber structure exhibited improved photocatalytic degradation and stability under light irradiation. Beside this work, Weng *et al.*[168] also reported synthesis of {001} facet dominated TiO_2 nanosheets on carbon fiber support (Fig. 20i-j). These hierarchical TiO_2 composites catalysts show enhanced photodegradation properties notably because of the high reactivity of {001} facets. Moreover, the authors remarked such hierarchical structure has shown to improve its reusability and more importantly, provide large surface area to fully expose the reactive facets.

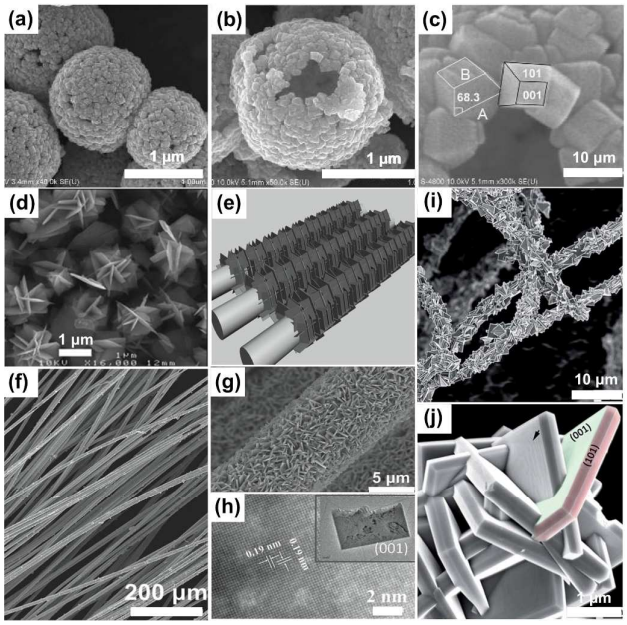

Fig. 20 SEM images of the fluoride-mediated TiO_2 samples: (a) image of a few microspheres; (b) a single microsphere showing its hollow nature; (c) a portion of the microsphere shell composed of nanosized polyhedra with exposed {001} facets. (d) SEM images of the flowerlike TiO2 nanosheets. (e) Schematic representation of the growth of TiO2 nanosheet arrays on carbon fibers. (f-g) SEM top-view images at different magnifications of uniform and dense arrays of TiO_2 nanosheets grown on carbon fibers. (h) TEM image of a TiO_2 nanosheet grown on a carbon fiber. Inset: Low-magnification image. (i-j) SEM images of TiO2 nanosheets grown on carbon fibers. Adapted from ref. 71, 162 and 167-168 with permission. Copyright Royal Society of Chemistry, American Chemical Society and WILEY-VCH Verlag GmbH & Co. KGaA, Weinheim.

Despite the rapid development of anatase TiO_2 with high energy facets for photocatalysis, challenges in synthetic route and reactivity prediction still persist. By and large, the synthesis methods reported for anatase TiO_2 crystals with high-energy facets are hazardous since they involve capping agents of F-based compounds which are highly corrosive. Thus it is desirable to develop new synthesis method which uses non-toxic and mild

capping agent. Also, though the general consensus was reached on the enhancement of photocatalytic reactivity with exposed {001} crystal facets, there are some conflicting reports on photocatalytic reactivity order of {010} > {101} > {001}.[169, 170] Importantly, various interrelated crystal variables should also be considered to predict the photocatalytic reaction of selective crystal facet. Nonetheless, the assembly of anatase building blocks into well-organized structure with highly exposed active crystal facets is crucial to the design of high photoredox reactivity of photocatalyst.

4.4 Mixed phase

The phase structure of TiO_2 is another important factor determining its photocatalytic performance. TiO_2 has mainly four polymorphs in nature, including anatase, rutile, brookite, and TiO_2(B). All four types of TiO_2 consist of TiO_6 octahedra, but differ in the distortion of the octahedron units and share edges and corners in different manners.[171] The photocatalytic activities of these different phases of TiO_2 are quite distinctive. Phase mixture of different polymorphs is known to have synergistic effect on increasing photocatalytic activity as compared to pure phases. However, for pure phases it is generally accepted that anatase exhibits a higher photocatalytic activity compared to rutile TiO_2. Few explanations have been extended to expound this phenomenon. Anatase has VB edge at higher energy level relative to redox potentials of adsorbed molecules which enhances the oxidation capability of holes by effective transfer of holes from the TiO_2 to adsorbed molecules.[172] Another explanation is that for a typical thermodynamically stable crystal, the dominant anatase {101} facet is of higher reactivity than the dominant rutile {110} facets.[173] Yet another explanation is that the difference in the charge diffusion length between the phases, i.e. anatase having a longer diffusion length promotes longer life-time of charge excitations and/or higher charge carrier mobilities in anatase than in rutile.[174] Evidently, it has been shown that P25 made up of a mixed phase of about 70% anatase and 30% rutile was indeed found to be more active than the pure anatase or rutile phase. For this purpose, various combinations of mixed phases were synthesized to increase photocatalytic activity. Construction of hierarchical structures is a rational means to realize mixed phases of TiO_2 photocatalysts. Thus far, numerous hierarchical TiO_2 nanocatalysts with mixed phases have been synthesized to enhance the photocatalytic property.

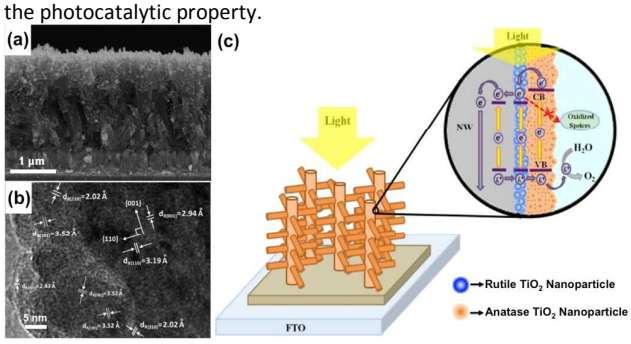

Fig. 21 (a) Cross-sectional-view SEM image of TiO_2 ND/RNP/ANP arrays. (b) TEM image of TiO_2 NW/RNP/ANP. (c) Schematic diagram illustrating the respective band positions and photogenerated charge separation in the hierarchical anatase/rutile TiO_2 nanostructured arrays. Adapted from ref. 175 with permission. Copyright 2013 American Chemical Society.

Among the mixed phases, the anatase and rutile phases are the most frequently studied photocatalysts of TiO_2. Hierarchical anatase-rutile TiO_2 has been prepared in a three-dimensional nanowire-nanoparticles array for photoelectrochemical water splitting.[175] The photoelectrode is composed of a one-dimensional rutile nanowire array with anatase nanoparticles (1.3-7.0 nm diameter) formed on the surface (Fig. 21a-b). The hierarchical TiO_2 structure of mixed phase enhances charge separation and suppresses charge recombination at the interfacial region between the electrode and water. The difference in the energy levels of anatase and rutile CB acts as an effective charge separator. Electron and hole transfer between the two phases can induce increased lifetimes of electrons and holes, as verified by the electrochemical impedance spectroscopy measurements, leading to higher photocatalytic activity (Fig. 21c). As explained, the photogenerated electrons in the CB preferentially transfer to the rutile nanostructure in the absence of a space charge region under the flat band condition. Through both hierarchical morphology and mixed phase interfacial energetics, a remarkable improvement in photocurrent density and high photoconversion efficiency are attained. Another anatase-rutile mixed-phase hierarchical structure consisting of zero-dimensional building blocks has reported for its high photocatalytic activity.[176] The hierarchical structure of interconnected nanoparticles forms relatively high surface area porous network. The mixed-phase titania photocatalysts in this work features tunable rutile ratio via sol–gel and controlled calcination process. As compared to conventional TiO_2 aggregates, such coexistence of the anatase and rutile phases hierarchical structure has shown superior photocatalytic performance, relative to either individual phase photocatalyst.

Among the crystalline TiO_2 phases, TiO_2(B) is far less common compared to other three phases. Owing to the lack of facile synthesis methods, TiO_2(B) and TiO_2(B) containing mixed phases are rarely studied as compared to the well-known anatase–rutile mixed phases. Recently, effective method to synthesize TiO_2(B) containing mixed phases have been demonstrated for photocatalytic applications. Wang *et al.*[177] reported hierarchical TiO_2 microspheres assembled by ultrathin nanoribbons of anatase-TiO_2(B) mixed phase. Upon increasing thermal treatment, the as-obtained nanoribbon (Fig. 22a-b) is transformed to TiO_2(B) at 400 °C (Fig. 22c-d), then into mixed phases of anatase at 500 °C (Fig. 22e-f) and finally to pure anatase phase (> 500 °C). According to the crystallographic orientations in Fig. 22e-f, it can be further deduced that an intimate interface is formed between (020) plane in anatase and the (020) plane of TiO_2(B). A coherent interface is observed between anatase and TiO_2(B) phases with closely matched lattice spacing of only 1.14% difference (0.3785 nm vs. 0.3741 nm). Therefore, it is believed that the epitaxial relationship between anatase and TiO_2(B) phases ensures a well-matched atomic arrangement of these mixed phases. Interestingly, besides the above lattice-match induced epitaxial relationship, the high energy facet of the anatase TiO_2 {001} is well-exposed. Such unique structure exhibits considerably high photocatalytic activity for organic degradation due to coexistence of exposed reactive facets and the offset of the band energy levels between different phases that facilitates the charge transfer and thus enhances the photocatalytic activity.

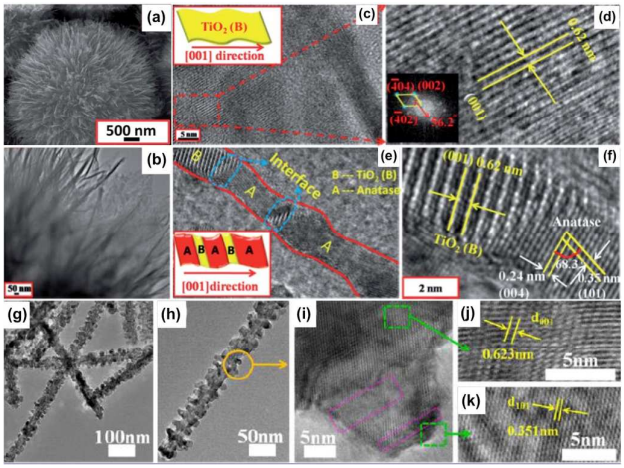

Fig. 22 (a) SEM and (b-f) TEM images of hierarchical TiO_2 microspheres. (g-k) TEM and HRTEM images of TiO_2(B)/anatase/rutile nanobelts with branch structures. Adapted from ref. 177-178 with permission. Copyright Royal Society of Chemistry and American Chemical Society.

Furthermore, hierarchical structure of TiO_2 nanobelts with branched nanorods consisting of three mixed phases, anatase-rutile-TiO_2(B) was reported by Sarkar *et al*. (Fig. 22g-k).[178] In detail, the nanobelt has uniform nanorods branches of 15 nm and width about 8 nm consisting of tri phases. The phase of the nanostructure was controlled precisely by different amount of titanium butoxide precursor and annealing temperatures respectively. The band bending effect at the interfaces of mixed-phases TiO_2(B), anatase, and rutile has been used to explain the improve photocatalytic effect. The CB of anatase phase is positioned at a higher energy level than that of rutile phase by about 0.20 eV, while the CB of anatase phase is at a lower energy level than that of TiO_2(B). When the three phases are in contact, the band edges differences aid interphase charge migration where the photogenerated electrons accumulate in the CB of rutile, while the holes at the TiO_2(B). This process reduces the recombination of the photogenerated charges and consequently improves the photocatalytic efficiency. The photocatalytic activity of these triphase nanobelts far exceeds that of single phase nanobelts.

Phase mixing approach is a promising strategy for enhancing charge separation in TiO_2 and hence increase photocatalytic reactivity. The origin of the improved photocatalysis performance is due to the potential difference established between disparate phases that promote efficient charge separation across the phase junction. The ability to synthesize and tailor both the TiO_2 phase type and composition ratio through precursor and temperature control has enabled systematic study of phase junction effect on photocatalysis. Various complementary time-resolved spectroscopies and electron paramagnetic resonance can be used to study the dynamics of photogenerated charge transfer to better understand the mechanism of phase junction in photocatalysis. [179-184]

4.5 Heterostructure

Hierarchical structure of two or more materials that forms heterostructure are often used to exploit the strengths of individual materials and compensate the respective shortcomings for improve photocatalysis properties. The construction of well-defined heterostructures by appropriate coupling of foreign components to host TiO_2 matrix is capable of improving photoactivity. Heterostructure of TiO_2 can effectively enhance photocatalysis through (i) extension of light absorption spectral range, (ii) enhancement of charge separation and (iii) suppression of charge recombination. Hierarchical heterostructure are usually fabricated by two main strategies namely direct/secondary assembly and loading/deposition of foreign components onto TiO_2 structures.

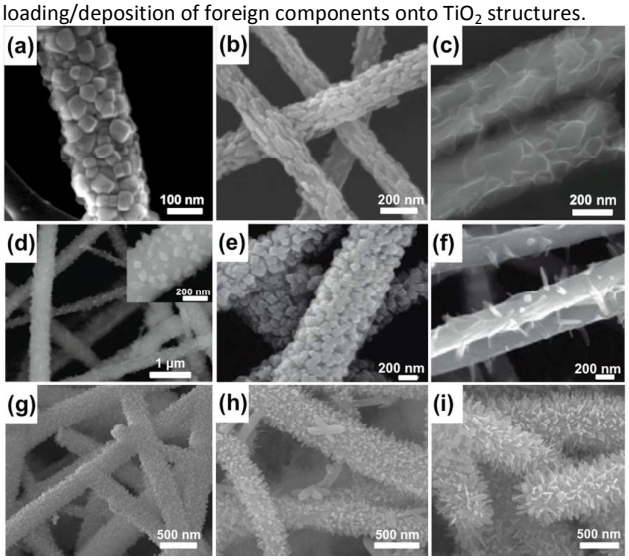

Fig. 23 SEM images of one-dimensional TiO_2 hierarchical structures (a) TiO_2 nanofiber with $SrTiO_3$ nanocubics heterostructures. (b) Wheat-grain textured TiO_2/CuO nanofibers. (c) Electrospun TiO_2 nanofiber with MoS_2 nanosheets. (d-f) SnO_2/TiO_2 heterostructures with SnO_2 nanoparticles, nanocrystals and nanorods architectures. (g-i) β-FeOOH/TiO_2 heterostructures with particles, needles to flakes. Adapted from ref. 39, 185-187 and 194 with permission. Copyright Nature Publishing Group, Elsevier, and American Chemical Society and WILEY-VCH Verlag GmbH & Co. KGaA, Weinheim.

In regard to the assembly of disparate material onto TiO_2 structures, direct electrospinning or secondary growth by hydrothermal synthesis on electrospun nanofiber are commonly used to fabricate one-dimensional heterostructures with controllable hierarchical features. Another attractive feature of using electrospinning method is its capability to prepare large scale mat or membrane nanofibers with potential of recycling. Different nanobuilding blocks ranging from nanoparticle, nanocubics, nanosheets, nanorods, nanoflakes have been reported as TiO_2 heterostructure with hierarchical design. TiO_2 nanofiber with $SrTiO_3$ nanocubic heterostructures are fabricated using the electrospinning and secondary hydrothermal technique (Fig. 23a).[185] The uniform distribution of $SrTiO_3$ cubic nanocrystals on the surface of TiO_2 nanofibers and their interfacial contact leads to beneficial separation of photogenerated carriers. The solar H_2 evolution test shows five times more than bare TiO_2 nanofibers. Our research group has recently reported TiO_2 nanofibers with nanoparticles heterostructure (Fig. 23b).[39] Unlike previous reports on conventional surface loading or growth of co-catalyst nanoparticles, direct amalgamation of co-catalyst during the electrospinning of TiO_2 nanofibers in our work ensures good stability and recyclability due to the resistance of the co-catalyst against leaching. The

resultant wheat grain-like textured heterostructure with embedded co-catalyst ensures high surface contact and intimate interface for enhanced photocatalytic H_2 generation of 16.8 times higher than that of bare TiO_2 nanofibers. Zhou *et al.*[186] reported electrospun TiO_2 nanofiber with hydrothermal growth of two dimensional building block of MoS_2 nanosheets that self-assembled on the surface of the nanofiber (Fig. 23c). The as-prepared heterostructures show high photocatalytic H_2 production and organic degradation as well as strong adsorption capabilities. Aside to the versatility of secondary hydrothermal growth on TiO_2 nanofibers, hierarchical heterostructures of various morphologies were reported by simply adjusting reaction parameters.[187] SnO_2/TiO_2 heterostructures with SnO_2 nanoparticles, nanocrystals and nanorods architectures were fabricated by changing $SnCl_4$ precursor concentration and reaction temperature (Fig. 23d-f). The photocatalytic studies demonstrated enhanced photocatalytic efficiency of photodegradation of SnO_2/TiO_2 heterostructures compare to bare TiO_2 nanofibers. Other hierarchical TiO_2 heterostructures with dissimilar materials and of various structures were synthesized using similar methods. SnS_2 nanosheets/TiO_2 nanofibers[188], ZnO nanocrystals/TiO_2 nanotube arrays[189], WO_3 nanoparticles/TiO_2 nanotube[190], ZnO nanorods/TiO_2 nanofibers[191], NiO_2/TiO_2 flowerlike spheres[192] and reduced graphene oxide (RGO) nanosheets/TiO_2 nanowires[193] hierarchical TiO_2 nanocomposite have been reported.

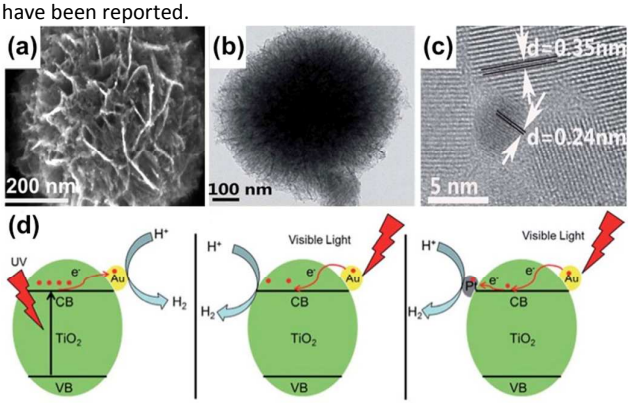

Fig. 24 (a) SEM and (b-c) TEM images of TiO2 spheres decorated with 2.43 wt% of Au nanoparticles (d) Possible photocatalytic H_2 production mechanism of TiO_2–Au under full spectrum light (left image) and visible light (λ > 420 nm), where middle image is TiO_2–Au and right image is TiO_2–Au and Pt nanoparticles. Adapted from ref. 201 with permission. Copyright 2015 Royal Society of Chemistry.

Other than the metal oxide based hierarchical heterostructure of dissimilar materials that could only be activated by UV light, the synthesis of more efficient visible-light driven multicomponent oxide photocatalysts with hierarchical heterostructure is a subject of considerable research interest. Our research group has recently reported hierarchical heterostructures of oxyhydroxide nanostructures on electrospun TiO_2 nanofibers. This work presented the versatility of tuning β-FeOOH structural design that cuts across zero-dimensional particles, one-dimensional needles to two-dimensional flakes (Fig. 23g-i). In addition, synthesizing such oxyhyroxide nanostructures presents the advantage of exhibiting similar functional performances to its oxides counterpart however, without the need to undergo any annealing step which leads to undesirable structural collapse or sintering. The as-obtained hierarchical branched nanostructures possess combined advantages of rapid charge transfer pathway for carrier collection, large surface area for more reaction sites, and excellent light trapping which are all favorable characteristics for enhanced photocatalytic degradation under visible light.[194] Similarly, Shang *et al.*[82] presented preparation of hierarchical nanofibrous mat that consist of heterostructure Bi_2WO_6 nanoplates growing aslant on the primary TiO_2 nanofibers. The hierarchical heterostructure exhibited enhanced visible photocatalytic activity of both organic compound in air and water. In general, when TiO_2 and the semiconductor are irradiated by light, photoinduced electron would be injected from the semiconductor with a more positive CB level to the other, while holes would be transferred from the semiconductor with a more negative VB level across to the one that is more positive. Thus, a spatial separation of photoinduced charges and suppression of charge recombination is achieved, which consequently enhances their lifetime. Furthermore, TiO_2 has limited UV light absorption, while narrow band gap semiconductor has a wider spectral light absorption. Hence, coupling of TiO_2 with a narrow band gap semiconductor can achieve an extension of light absorption.

Another popular method of synthesizing heterostructure involves straightforward and simple loading of co-catalyst onto hierarchical TiO_2 structure. The mass loading and thickness of the deposited co-catalyst onto the TiO_2 surface are usually optimized since high mass loading or too thick co-catalyst film could block the light incident onto TiO_2 as co-catalysts are typically opaque. In general, noble metals, such as Pt,[195] Pd,[196] Au,[197] Rh,[198] Ru,[199] and Ag[200] have often been used as efficient co-catalysts. The work function of most metal is larger than that of TiO_2 (4.2 eV), hence readily promotes the electron transfer from CB of TiO_2 to metal. The electron trapping ability of the metal increases with the work function as such Pt, the highest workfunction is noted as the best proton reduction cocatalyst amongst the noble metals. A Schottky barrier is formed at the interface when TiO_2 semiconductor is coupled with metal. The Schottky barrier will drive electron migration from TiO_2 to the noble metal up until a thermodynamic equilibrium state is reached, that is, when the Fermi levels are aligned. Subsequent exposure to light irradiation will cause the shift of TiO_2 Fermi level to a new quasi-Fermi level in which photogenerated electrons are rapidly transferred from TiO_2 to Pt particles while the holes remained on the TiO_2 hence decreasing the recombination rate of electron–hole pairs. Zhang *et al.*[201] reported hierarchical heterostructure TiO_2 spheres composed of nanosheets that were loaded with Au nanoparticles through anchor molecules (Fig. 24a-c). Different light irradiation scenarios were discussed as such under UV light, photoinduced electrons migrate to Au nanoparticles of higher workfunction that TiO_2 (Fig. 24d, left), while under visible light, the hot electrons generated in Au nanoparticles due to localized surface plasmon resonance effect will inject electrons to the TiO_2(Fig. 24d, middle). Furthermore, dual co-catalyst loading of Pt and Au nanoparticles on the TiO_2 which further improves the photocatalytic H_2 production rates observed under UV to visible light irradiation is greatly enhanced with the presence of heterojunctions (Fig. 24d, right).

Conclusions

As discussed, wide band gap semiconductor TiO_2 is low cost and stable but inherently exhibits ineffective visible light absorption. Furthermore, charge recombination is another crucial factor that limits the solar energy conversion efficiency of TiO_2 photocatalysts. Despite these challenges, TiO_2 based photocatalysts continues to be the focus of photocatalytic studies since the aforementioned drawbacks are surmountable with synergistic combination of structural and electronic strategies. Here we have reviewed the background of critical design of photocatalyst/photoelectrode materials, a key towards marked improvement in solar energy conversion efficiency of TiO_2 based photocatalysts. We have highlighted TiO_2 photocatalysts with well-defined structural design and the material composition exploitations that contribute to significant improvement in vital processes and attributes such as light absorption, photostability, charge-carrier dynamics, surface area etc. In our opinions, the future generation photocatalyst will be of increasing complexity in terms of structural architecture as well as materials constituents. Sophisticated structural and materials hybridization can possibly be achieved through controlled synthesis and solid solution (alloying) of intrinsically narrow-band-gap materials for tunable band gap as shown in our recent publications. These efforts should coincide with the exploration of green and facile synthesis along with earth-abundant materials usage of appropriate energy alignment to address the ubiquitous cost and sustainability issues. Other fundamental gaps to be bridged include in-depth understanding of kinetics and dynamics of photoreactivity and other photocatalytic mechanistic studies at the nanometer and atomic levels using complementary computation, spectroscopy, microscopy and electrochemical techniques. With all the challenges of TiO_2 photocatalyst overcome, we can expect TiO_2-based photocatalyst to play an important role in the future clean fuel H_2 production and environmental remediation applications.

Acknowledgements

This work is supported by the MOE R-263-000-B38-112, R-263-000-B63-112 and A*star R-263-000-A96-305.

References

1. M.-Q. Yang, N. Zhang, M. Pagliaro and Y.-J. Xu, *Chem. Soc. Rev.*, 2014, 43, 8240-8254.
2. V. M. Daskalaki, M. Antoniadou, G. Li Puma, D. I. Kondarides and P. Lianos, *Environ. Sci. Technol.*, 2010, 44, 7200-7205.
3. M. Stylidi, D. I. Kondarides and X. E. Verykios, *Int. J. Photoenergy*, 2003, DOI: 10.1155/s1110662x0300014x.
4. A. Fujishima and K. Honda, *Nature*, 1972, 238, 37-38.
5. N. Strataki, M. Antoniadou, V. Dracopoulos and P. Lianos, *Catalysis Today*, 2010, 151, 53-57.
6. P. Panagiotopoulou and D. I. Kondarides, *J. Catal.*, 2004, 225, 327-336.
7. S. Liu, Z.-R. Tang, Y. Sun, J. C. Colmenares and Y.-J. Xu, *Chem. Soc. Rev.*, 2015, DOI: 10.1039/C4CS00408F.
8. N. Zhang, S. Liu and Y.-J. Xu, *Nanoscale*, 2012, 4, 2227-2238.
9. J. Li and N. Wu, *Catal. Sci. Technol.*, 2015, 5, 1360-1384.
10. M. K. a. I. Okura, *Photocatalysis: Science and Technology*, Springer, 2002.
11. R. P. a. J. J. A. J. Bard, *Standard Potentials in Aqueous Solution*, Taylor & Francis, 1985.
12. V. Subramanian, E. E. Wolf and P. V. Kamat, *J. Am. Chem. Soc.*, 2004, 126, 4943-4950.
13. D. B. Ingram and S. Linic, *J. Am. Chem. Soc.*, 2011, 133, 5202-5205.
14. A. Tanaka, S. Sakaguchi, K. Hashimoto and H. Kominami, *ACS Catal.*, 2013, 3, 79-85.
15. H. Liu, J. Yuan and W. Shangguan, *Energy Fuels*, 2006, 20, 2289-2292.
16. X.-F. Wu, Y.-F. Chen, J.-M. Yoon and Y.-T. Yu, *Mater. Lett.*, 2010, 64, 2208-2210.
17. F.-X. Xiao, S.-F. Hung, J. Miao, H.-Y. Wang, H. Yang and B. Liu, *Small*, 2015, 11, 553-553.
18. M. Ye, J. Gong, Y. Lai, C. Lin and Z. Lin, *J. Am. Chem. Soc.*, 2012, 134, 15720-15723.
19. F. Lakadamyali and E. Reisner, *Chem. Commun.*, 2011, 47, 1695-1697.
20. M. Yin, S. Ma, C. Wu and Y. Fan, *RSC Adv.*, 2015, 5, 1852-1858.
21. P. D. Tran, L. Xi, S. K. Batabyal, L. H. Wong, J. Barber and J. S. Chye Loo, *Phys. Chem. Chem. Phys.*, 2012, 14, 11596-11599.
22. Y. Xia and L. Yin, *Phys. Chem. Chem. Phys.*, 2013, 15, 18627-18634.
23. M. A. Ahmed, E. E. El-Katori and Z. H. Gharni, *J. Alloys Compd.*, 2013, 553, 19-29.
24. F. Mou, L. Xu, H. Ma, J. Guan, D.-r. Chen and S. Wang, *Nanoscale*, 2012, 4, 4650-4657.
25. W.-H. Hung, T.-M. Chien and C.-M. Tseng, *J. Phys. Chem. C*, 2014, 118, 12676-12681.
26. Z. Wu, Y. Wang, L. Sun, Y. Mao, M. Wang and C. Lin, *J. Mater. Chem. A*, 2014, 2, 8223-8229.
27. A. K. Agegnehu, C.-J. Pan, J. Rick, J.-F. Lee, W.-N. Su and B.-J. Hwang, *J. Mater. Chem.*, 2012, 22, 13849-13854.
28. L. N. Quan, Y. H. Jang, K. A. Stoerzinger, K. J. May, Y. J. Jang, S. T. Kochuveedu, Y. Shao-Horn and D. H. Kim, *Phys. Chem. Chem. Phys.*, 2014, 16, 9023-9030.
29. C. H. Kim, B.-H. Kim and K. S. Yang, *Carbon*, 2012, 50, 2472-2481.
30. S. Xie, H. Su, W. Wei, M. Li, Y. Tong and Z. Mao, *J. Mater. Chem. A*, 2014, 2, 16365-16368.
31. B. Jiang, C. Tian, Q. Pan, Z. Jiang, J.-Q. Wang, W. Yan and H. Fu, *J. Phys. Chem. C*, 2011, 115, 23718-23725.
32. S. D. Perera, R. G. Mariano, K. Vu, N. Nour, O. Seitz, Y. Chabal and K. J. Balkus, *ACS Catal.*, 2012, 2, 949-956.
33. N. Zhang, Y. Zhang and Y.-J. Xu, *Nanoscale*, 2012, 4, 5792-5813.
34. N. Zhang, M.-Q. Yang, Z.-R. Tang and Y.-J. Xu, *ACS Nano*, 2014, 8, 623-633.
35. G. D. Moon, J. B. Joo, I. Lee and Y. Yin, *Nanoscale*, 2014, 6, 12002-12008.
36. G. Yang, Z. Yan and T. Xiao, *Appl. Surf. Sci.*, 2012, 258, 8704-8712.
37. V. Pandit, S. Arbuj, R. Hawaldar, P. Kshirsagar, U. Mulik, S. Gosavi, C.-J. Park and B. Kale, *J. Mater. Chem. A*, 2015, 3, 4338-4344.
38. J. Wang, X. Li, X. Li, J. Zhu and H. Li, *Nanoscale*, 2013, 5, 1876-1881.
39. L. Zhu, M. Hong and G. W. Ho, *Nano Energy*, 2015, 11, 28-37.
40. S. Y. Chae, M. K. Park, S. K. Lee, T. Y. Kim, S. K. Kim and W. I. Lee, *Chem. Mater.*, 2003, 15, 3326-3331.
41. A. N. Banerjee, *Nanotechnol Sci Appl.*, 2011, 4, 35-65.
42. J. Zhu and M. Zäch, *Curr. Opin. Colloid Interface Sci.*, 2009, 14, 260-269.
43. S.-Y. Lee and S.-J. Park, *J. Ind. Eng. Chem.*, 2013, 19, 1761-1769.

44. A. Fujishima, X. Zhang and D. A. Tryk, *Surf. Sci. Rep.*, 2008, 63, 515-582.
45. H. Zhang and J. F. Banfield, *J. Phys. Chem. B*, 2000, 104, 3481-3487.
46. F. Xiao, *J. Mater. Chem.*, 2012, 22, 7819-7830.
47. J. Fan, L. Zhao, J. Yu and G. Liu, *Nanoscale*, 2012, 4, 6597-6603.
48. J. Yu, G. Dai and B. Cheng, *J. Phys. Chem. C*, 2010, 114, 19378-19385.
49. T. J. Wong, F. J. Lim, M. Gao, G. H. Lee and G. W. Ho, *Catal. Sci. Technol.*, 2013, 3, 1086-1093.
50. T. Peng, A. Hasegawa, J. Qiu and K. Hirao, *Chem. Mater.*, 2003, 15, 2011-2016.
51. X. Zhang, T. Zhang, J. Ng and D. D. Sun, *Adv. Funct. Mater.*, 2009, 19, 3731-3736.
52. Y. Wang, L. Zhang, K. Deng, X. Chen and Z. Zou, *J. Phys. Chem. C*, 2007, 111, 2709-2714.
53. H. Xu, F. Jia, Z. Ai and L. Zhang, *Cryst. Growth Des.*, 2007, 7, 1216-1219.
54. H. J. Yun, H. Lee, J. B. Joo, W. Kim and J. Yi, *J. Phys. Chem. C*, 2009, 113, 3050-3055.
55. J. Yu, Q. Xiang and M. Zhou, *Appl. Catal., B*, 2009, 90, 595-602.
56. I. M. Arabatzis and P. Falaras, *Nano Lett.*, 2003, 3, 249-251.
57. A. Yamamoto and H. Imai, *J. Catal.*, 2004, 226, 462-465.
58. W. Zhou, W. Li, J.-Q. Wang, Y. Qu, Y. Yang, Y. Xie, K. Zhang, L. Wang, H. Fu and D. Zhao, *J. Am. Chem. Soc.*, 2014, 136, 9280-9283.
59. S. Lee, K. Teshima, M. Fujisawa, S. Fujii, M. Endo and S. Oishi, *Phys. Chem. Chem. Phys.*, 2009, 11, 3628-3633.
60. J. B. Joo, M. Dahl, N. Li, F. Zaera and Y. Yin, *Energy Environ. Sci.*, 2013, 6, 2082-2092.
61. A. A. Ismail and D. W. Bahnemann, *J. Mater. Chem.*, 2011, 21, 11686-11707.
62. D. Y. C. Leung, X. Fu, C. Wang, M. Ni, M. K. H. Leung, X. Wang and X. Fu, *ChemSusChem*, 2010, 3, 681-694.
63. K. Takanabe and K. Domen, *ChemCatChem*, 2012, 4, 1485-1497.
64. X.-Q. Gong and A. Selloni, *J. Phys. Chem. B*, 2005, 109, 19560-19562.
65. A. Vittadini, A. Selloni, F. P. Rotzinger and M. Grätzel, *Phys. Rev. Lett.*, 1998, 81, 2954-2957.
66. H. G. Yang, C. H. Sun, S. Z. Qiao, J. Zou, G. Liu, S. C. Smith, H. M. Cheng and G. Q. Lu, *Nature*, 2008, 453, 638-641.
67. X. Han, Q. Kuang, M. Jin, Z. Xie and L. Zheng, *J. Am. Chem. Soc.*, 2009, 131, 3152-3153.
68. H. G. Yang, G. Liu, S. Z. Qiao, C. H. Sun, Y. G. Jin, S. C. Smith, J. Zou, H. M. Cheng and G. Q. Lu, *J. Am. Chem. Soc.*, 2009, 131, 4078-4083.
69. W. Yang, J. Li, Y. Wang, F. Zhu, W. Shi, F. Wan and D. Xu, *Chem. Commun.*, 2011, 47, 1809-1811.
70. C. Hu, X. Zhang, W. Li, Y. Yan, G. Xi, H. Yang, J. Li and H. Bai, *J. Mater. Chem. A*, 2014, 2, 2040-2043.
71. W. Guo, F. Zhang, C. Lin and Z. L. Wang, *Adv. Mater.*, 2012, 24, 4761-4764.
72. J. B. Joo, I. Lee, M. Dahl, G. D. Moon, F. Zaera and Y. Yin, *Adv. Funct. Mater.*, 2013, 23, 4246-4254.
73. J. Zhang, Z. Zhu, Y. Tang and X. Feng, *J. Mater. Chem. A*, 2013, 1, 3752-3756.
74. B. Wang, X.-Y. Lu, L. K. Yu, J. Xuan, M. K. H. Leung and H. Guo, *CrystEngComm*, 2014, 16, 10046-10055.
75. S. Shang, X. Jiao and D. Chen, *ACS Appl. Mater. Inter.*, 2012, 4, 860-865.
76. H. Zhang, G. Du, W. Lu, L. Cheng, X. Zhu and Z. Jiao, *CrystEngComm*, 2012, 14, 3793-3801.
77. W. Dong, Y. Sun, C. W. Lee, W. Hua, X. Lu, Y. Shi, S. Zhang, J. Chen and D. Zhao, *J. Am. Chem. Soc.*, 2007, 129, 13894-13904.
78. M. Wu, J. Jin, J. Liu, Z. Deng, Y. Li, O. Deparis and B.-L. Su, *J. Mater. Chem. A*, 2013, 1, 15491-15500.
79. R. Zhang, D. Shen, M. Xu, D. Feng, W. Li, G. Zheng, R. Che, A. A. Elzatahry and D. Zhao, *Adv. Energy Mater.*, 2014, 4, n/a-n/a.
80. K. Xia, D. Ferguson, Y. Djaoued, J. Robichaud, N. Tchoukanova, R. Brüning and E. McCalla, *Appl. Catal., A.*, 2010, 387, 231-241.
81. M. Ge, J. W. Li, L. Liu and Z. Zhou, *Ind. Eng. Chem. Res.*, 2011, 50, 6681-6687.
82. M. Shang, W. Wang, L. Zhang, S. Sun, L. Wang and L. Zhou, *J. Phys. Chem. C*, 2009, 113, 14727-14731.
83. H. Bai, Z. Liu and D. D. Sun, *Int. J. Hydrogen Energy*, 2012, 37, 13998-14008.
84. T.-D. Nguyen-Phan, E.-S. Oh, M. Chhowalla, T. Asefa and E. W. Shin, *J. Mater. Chem. A*, 2013, 1, 7690-7701.
85. J. H. Pan, H. Dou, Z. Xiong, C. Xu, J. Ma and X. S. Zhao, *J. Mater. Chem.*, 2010, 20, 4512-4528.
86. X. Wu, G. Q. Lu and L. Wang, *Energy Environ. Sci.*, 2011, 4, 3565-3572.
87. J. B. Joo, Q. Zhang, I. Lee, M. Dahl, F. Zaera and Y. Yin, *Adv. Funct. Mater.*, 2012, 22, 166-174.
88. J. Lu, P. Zhang, A. Li, F. Su, T. Wang, Y. Liu and J. Gong, *Chem. Commun.*, 2013, 49, 5817-5819.
89. D. P. Wang and H. C. Zeng, *Chem. Mater.*, 2009, 21, 4811-4823.
90. N. Zhang, S. Liu, X. Fu and Y.-J. Xu, *J. Phys. Chem. C*, 2011, 115, 9136-9145.
91. M. Gao, C. K. N. Peh, Y. Pan, Q.-H. Xu and G. W. Ho, *Nanoscale*, 2014, 6, 12655-12664.
92. H. Xu, G. Li, N. Liu, K. Zhu, G. Zhu and S. Jin, *Mater. Lett.*, 2015, 142, 324-327.
93. I. Lee, Q. Zhang, J. Ge, Y. Yin and F. Zaera, *Nano Res.*, 2011, 4, 115-123.
94. J. Ge, Q. Zhang, T. Zhang and Y. Yin, *Angew. Chem. Int. Ed.*, 2008, 47, 8924-8928.
95. Q. Zhang, I. Lee, J. Ge, F. Zaera and Y. Yin, *Adv. Funct. Mater.*, 2010, 20, 2201-2214.
96. Q. Zhang, D. Q. Lima, I. Lee, F. Zaera, M. Chi and Y. Yin, *Angew. Chem. Int. Ed.*, 2011, 123, 7226-7230.
97. R. Daghrir, P. Drogui and D. Robert, *Ind. Eng. Chem. Res.*, 2013, 52, 3581-3599.
98. S. Hernández, V. Cauda, A. Chiodoni, S. Dallorto, A. Sacco, D. Hidalgo, E. Celasco and C. F. Pirri, *ACS Appl. Mater. Inter.*, 2014, 6, 12153-12167.
99. Y. Li, S. Ji, Y. Gao, H. Luo and M. Kanehira, *Sci. Rep.*, 2013, 3.
100. A. Small, S. Hong and D. Pine, *Journal of Polymer Science Part B: Polymer Physics*, 2005, 43, 3534-3548.
101. S. Son, S. H. Hwang, C. Kim, J. Y. Yun and J. Jang, *ACS Appl. Mater. Inter.*, 2013, 5, 4815-4820.
102. S. H. Hwang, D. H. Shin, J. Yun, C. Kim, M. Choi and J. Jang, *Chem. Eur. J.*, 2014, 20, 4439-4446.
103. T. Zhao, Z. Liu, K. Nakata, S. Nishimoto, T. Murakami, Y. Zhao, L. Jiang and A. Fujishima, *J. Mater. Chem.*, 2010, 20, 5095-5099.
104. S. Li, J. Chen, F. Zheng, Y. Li and F. Huang, *Nanoscale*, 2013, 5, 12150-12155.
105. J. B. Yoo, H. J. Yoo, B. W. Lim, K. H. Lee, M. H. Kim, D. Kang and N. H. Hur, *ChemSusChem*, 2012, 5, 2334-2340.
106. H. Li, Z. Bian, J. Zhu, D. Zhang, G. Li, Y. Huo, H. Li and Y. Lu, *J. Am. Chem. Soc.*, 2007, 129, 8406-8407.
107. Y. Chen and D. D. Dionysiou, *Appl. Catal., B*, 2006, 69, 24-33.
108. Y. Kondo, H. Yoshikawa, K. Awaga, M. Murayama, T. Mori, K. Sunada, S. Bandow and S. Iijima, *Langmuir*, 2008, 24, 547-550.

109. M.-C. Tsai, J.-Y. Lee, P.-C. Chen, Y.-W. Chang, Y.-C. Chang, M.-H. Yang, H.-T. Chiu, I. N. Lin, R.-K. Lee and C.-Y. Lee, *Appl. Catal., B*, 2014, 147, 499-507.
110. Y. Tang, W. Di, X. Zhai, R. Yang and W. Qin, *ACS Catal.*, 2013, 3, 405-412.
111. W. Wang, M. Ding, C. Lu, Y. Ni and Z. Xu, *Appl. Catal., B*, 2014, 144, 379-385.
112. W. Qin, D. Zhang, D. Zhao, L. Wang and K. Zheng, *Chem. Commun.*, 2010, 46, 2304-2306.
113. G. Chen, H. Agren, T. Y. Ohulchanskyy and P. N. Prasad, *Chem. Soc. Rev.*, 2015, 44, 1680-1713.
114. L. T. Su, S. K. Karuturi, J. Luo, L. Liu, X. Liu, J. Guo, T. C. Sum, R. Deng, H. J. Fan, X. Liu and A. I. Y. Tok, *Adv. Mater.*, 2013, 25, 1603-1607.
115. Y. Zhang and Z. Hong, *Nanoscale*, 2013, 5, 8930-8933.
116. T. W. Odom and G. C. Schatz, *Chem. Rev.*, 2011, 111, 3667-3668.
117. M. K. Kumar, S. Krishnamoorthy, L. K. Tan, S. Y. Chiam, S. Tripathy and H. Gao, *ACS Catal.*, 2011, 1, 300-308.
118. N. Zhou, L. Polavarapu, N. Gao, Y. Pan, P. Yuan, Q. Wang and Q.-H. Xu, *Nanoscale*, 2013, 5, 4236-4241.
119. X. Zhang, Y. Zhu, X. Yang, S. Wang, J. Shen, B. Lin and C. Li, *Nanoscale*, 2013, 5, 3359-3366.
120. J.-J. Chen, J. C. S. Wu, P. C. Wu and D. P. Tsai, *J. Phys. Chem. C*, 2012, 116, 26535-26542.
121. T. Butburee, Y. Bai, J. Pan, X. Zong, C. Sun, G. Liu and L. Wang, *J. Mater. Chem. A*, 2014, 2, 12776-12784.
122. X. Peng, A. C. Santulli, E. Sutter and S. S. Wong, *Chem. Sci.*, 2012, 3, 1262-1272.
123. X. Qu, Y. Hou, C. Wang, F. Du and L. Cao, *RSC Adv.*, 2015, 5, 5307-5311.
124. T. Hirakawa and P. V. Kamat, *J. Am. Chem. Soc.*, 2005, 127, 3928-3934.
125. P. Zhang, C. Shao, Z. Zhang, M. Zhang, J. Mu, Z. Guo and Y. Liu, *Nanoscale*, 2011, 3, 2943-2949.
126. R. J. Dillon, J.-B. Joo, F. Zaera, Y. Yin and C. J. Bardeen, *Phys. Chem. Chem. Phys.*, 2013, 15, 1488-1496.
127. A. Islam, Y. Cho, U. H. Yim, W. J. Shim, Y. H. Kim and S. Kim, *J. Hazard. Mater.*, 2013, 263, Part 2, 404-411.
128. H. Wang, X. Fei, L. Wang, Y. Li, S. Xu, M. Sun, L. Sun, C. Zhang, Y. Li, Q. Yang and Y. Wei, *New J. Chem.*, 2011, 35, 1795-1802.
129. W. Su, T. Zhang, L. Li, J. Xing, M. He, Y. Zhong and Z. Li, *RSC Adv.*, 2014, 4, 8901-8906.
130. Y. Zhang, X. Yu, Y. Jia, Z. Jin, J. Liu and X. Huang, *Eur. J. Inorg. Chem.*, 2011, 2011, 5096-5104.
131. W. Wu, J. Changzhong and V. A. L. Roy, *Nanoscale*, 2015, 7, 38-58.
132. J. Zhou, F. Ren, S. Zhang, W. Wu, X. Xiao, Y. Liu and C. Jiang, *J. Mater. Chem. A*, 2013, 1, 13128-13138.
133. J. Su, Y. Zhang, S. Xu, S. Wang, H. Ding, S. Pan, G. Wang, G. Li and H. Zhao, *Nanoscale*, 2014, 6, 5181-5192.
134. P. Gao, A. Li, D. D. Sun and W. J. Ng, *J. Hazard. Mater.*, 2014, 279, 96-104.
135. Z. Sun, J. H. Kim, Y. Zhao, F. Bijarbooneh, V. Malgras, Y. Lee, Y.-M. Kang and S. X. Dou, *J. Am. Chem. Soc.*, 2011, 133, 19314-19317.
136. H. Li, H. Yu, L. Sun, J. Zhai and X. Han, *Nanoscale*, 2015, 7, 1610-1615.
137. Z. Zheng, B. Huang, X. Qin, X. Zhang and Y. Dai, *Chem. Eur. J.*, 2010, 16, 11266-11270.
138. Q. Chen, C. Chen, H. Ji, W. Ma and J. Zhao, *RSC Adv.*, 2013, 3, 17559-17566.
139. L. Zhang, L. Chen, L. Chen and G. Zhu, *RSC Adv.*, 2014, 4, 54463-54468.
140. H. Ming, Z. Ma, H. Huang, S. Lian, H. Li, X. He, H. Yu, K. Pan, Y. Liu and Z. Kang, *Chem. Commun.*, 2011, 47, 8025-8027.
141. Q. Zhang, J.-B. Joo, Z. Lu, M. Dahl, D. L. Oliveira, M. Ye and Y. Yin, *Nano Res.*, 2011, 4, 103-114.
142. B. Liu, K. Nakata, M. Sakai, H. Saito, T. Ochiai, T. Murakami, K. Takagi and A. Fujishima, *Catal. Sci. Technol.*, 2012, 2, 1933-1939.
143. H. Bai, L. Liu, Z. Liu and D. D. Sun, *Water Res.*, 2013, 47, 4126-4138.
144. T. Zhu, J. Li and Q. Wu, *ACS Appl. Mater. Inter.*, 2011, 3, 3448-3453.
145. Y. Tang, D. Gong, Y. Lai, Y. Shen, Y. Zhang, Y. Huang, J. Tao, C. Lin, Z. Dong and Z. Chen, *J. Mater. Chem.*, 2010, 20, 10169-10178.
146. W. Li, Z. Wu, J. Wang, A. A. Elzatahry and D. Zhao, *Chem. Mater.*, 2014, 26, 287-298.
147. H. Bai, X. Li, C. Hu, X. Zhang, J. Li, Y. Yan and G. Xi, *Sci. Rep.*, 2013, 3.
148. Y. Sakatani, D. Grosso, L. Nicole, C. Boissiere, G. J. de A. A. Soler-Illia and C. Sanchez, *J. Mater. Chem.*, 2006, 16, 77-82.
149. J. Du, X. Lai, N. Yang, J. Zhai, D. Kisailus, F. Su, D. Wang and L. Jiang, *ACS Nano*, 2011, 5, 590-596.
150. H. Liu, QibinZhao, H. Zhou, J. Ding, D. Zhang, H. Zhu and T. Fan, *Phys. Chem. Chem. Phys.*, 2011, 13, 10872-10876.
151. X. Liu, S. Zhu, D. Zhang and Z. Chen, *Mater. Lett.*, 2010, 64, 2745-2747.
152. X. Li, T. Fan, H. Zhou, S.-K. Chow, W. Zhang, D. Zhang, Q. Guo and H. Ogawa, *Adv. Funct. Mater.*, 2009, 19, 45-56.
153. B. Liu, X. Zhao, K. Nakata and A. Fujishima, *J. Mater. Chem. A*, 2013, 1, 4993-5000.
154. Q. Yang, M. Li, J. Liu, W. Shen, C. Ye, X. Shi, L. Jiang and Y. Song, *J. Mater. Chem. A*, 2013, 1, 541-547.
155. M. C. Tsai, M. H. Yang, Y. W. Chang, J. K. Tzeng, C. Y. Lee, H. T. Chiu, H. C. Chen and I. N. Lin, *Mater. Chem. Phys.*, 2013, 143, 60-64.
156. B. Chen, J. A. Beach, D. Maurya, R. B. Moore and S. Priya, *RSC Adv.*, 2014, 4, 29443-29449.
157. F. Su, T. Wang, R. Lv, J. Zhang, P. Zhang, J. Lu and J. Gong, *Nanoscale*, 2013, 5, 9001-9009.
158. I. S. Cho, Z. Chen, A. J. Forman, D. R. Kim, P. M. Rao, T. F. Jaramillo and X. Zheng, *Nano Lett.*, 2011, 11, 4978-4984.
159. S. Lou, X. Guo, T. Fan and D. Zhang, *Energy Environ. Sci.*, 2012, 5, 9195-9216.
160. M. Lazzeri, A. Vittadini and A. Selloni, *Phys. Rev. B*, 2002, 65, 119901.
161. S. Liu, J. Yu and M. Jaroniec, *Chem. Mater.*, 2011, 23, 4085-4093.
162. S. Liu, J. Yu and M. Jaroniec, *J. Am. Chem. Soc.*, 2010, 132, 11914-11916.
163. C. Z. Wen, H. B. Jiang, S. Z. Qiao, H. G. Yang and G. Q. Lu, *J. Mater. Chem.*, 2011, 21, 7052-7061.
164. M. Liu, L. Piao, W. Lu, S. Ju, L. Zhao, C. Zhou, H. Li and W. Wang, *Nanoscale*, 2010, 2, 1115-1117.
165. H. Li, Y. Zeng, T. Huang, L. Piao, Z. Yan and M. Liu, *Chem. Eur. J.*, 2012, 18, 7525-7532.
166. J. Miao and B. Liu, *RSC Adv.*, 2013, 3, 1222-1226.
167. W. Q. Fang, J. Z. Zhou, J. Liu, Z. G. Chen, C. Yang, C. H. Sun, G. R. Qian, J. Zou, S. Z. Qiao and H. G. Yang, *Chem. Eur. J.*, 2011, 17, 1423-1427.
168. B. Weng, F. Xu and J. Xu, *RSC Adv.*, 2014, 4, 56682-56689.
169. L. Ye, J. Mao, T. Peng, L. Zan and Y. Zhang, *Phys. Chem. Chem. Phys.*, 2014, 16, 15675-15680.
170. H. Xu, P. Reunchan, S. Ouyang, H. Tong, N. Umezawa, T. Kako and J. Ye, *Chem. Mater.*, 2013, 25, 405-411.
171. L. Sang, Y. Zhao and C. Burda, *Chem. Rev.*, 2014, 114, 9283-9318.
172. M. Batzill, *Energy Environ. Sci.*, 2011, 4, 3275-3286.
173. A. Y. Ahmed, T. A. Kandiel, T. Oekermann and D. Bahnemann, *J. Phys. Chem. Lett.*, 2011, 2, 2461-2465.

174. T. Luttrell, S. Halpegamage, J. Tao, A. Kramer, E. Sutter and M. Batzill, *Sci. Rep.*, 2014, 4, 4043.
175. J.-S. Yang, W.-P. Liao and J.-J. Wu, *ACS Appl. Mater. Inter.*, 2013, 5, 7425-7431.
176. L. Cao, D. Chen, W. Li and R. A. Caruso, *ACS Appl. Mater. Inter.*, 2014, 6, 13129-13137.
177. C. Wang, X. Zhang and Y. Liu, *Nanoscale*, 2014, 6, 5329-5337.
178. D. Sarkar and K. K. Chattopadhyay, *ACS Appl. Mater. Inter.*, 2014, 6, 10044-10059.
179. S. Leytner and J. T. Hupp, *Chem. Phys. Lett.*, 2000, 330, 231-236.
180. H. Nakajima, T. Mori, Q. Shen and T. Toyoda, *Chem. Phys. Lett.*, 2005, 409, 81-84.
181. D. C. Hurum, K. A. Gray, T. Rajh and M. C. Thurnauer, *J. Phys. Chem. B*, 2005, 109, 977-980.
182. D. C. Hurum, A. G. Agrios, K. A. Gray, T. Rajh and M. C. Thurnauer, *J. Phys. Chem. B*, 2003, 107, 4545-4549.
183. G. Li and K. A. Gray, *Chem. Phys.*, 2007, 339, 173-187.
184. D. C. Hurum, A. G. Agrios, S. E. Crist, K. A. Gray, T. Rajh and M. C. Thurnauer, *J. Electron. Spectrosc. Relat. Phenom.*, 2006, 150, 155-163.
185. H. Bai, J. Juay, Z. Liu, X. Song, S. S. Lee and D. D. Sun, *Appl. Catal., B*, 2012, 125, 367-374.
186. W. Zhou, Z. Yin, Y. Du, X. Huang, Z. Zeng, Z. Fan, H. Liu, J. Wang and H. Zhang, *Small*, 2013, 9, 140-147.
187. C. Wang, C. Shao, X. Zhang and Y. Liu, *Inorg. Chem.*, 2009, 48, 7261-7268.
188. Z. Zhang, C. Shao, X. Li, Y. Sun, M. Zhang, J. Mu, P. Zhang, Z. Guo and Y. Liu, *Nanoscale*, 2013, 5, 606-618.
189. F.-X. Xiao, *ACS Appl. Mater. Inter.*, 2012, 4, 7055-7063.
190. B. Lu, X. Li, T. Wang, E. Xie and Z. Xu, *J. Mater. Chem. A*, 2013, 1, 3900-3906.
191. T. J. Athauda, J. G. Neff, L. Sutherlin, U. Butt and R. R. Ozer, *ACS Appl. Mater. Inter.*, 2012, 4, 6917-6926.
192. J. Yu, W. Wang and B. Cheng, *Chem. Asian J.*, 2010, 5, 2499-2506.
193. X. Cao, G. Tian, Y. Chen, J. Zhou, W. Zhou, C. Tian and H. Fu, *J. Mater. Chem. A*, 2014, 2, 4366-4374.
194. T. Zhu, W. Li Ong, L. Zhu and G. Wei Ho, *Sci. Rep.*, 2015, 5.
195. J. Yu, L. Qi and M. Jaroniec, *J. Phys. Chem. C*, 2010, 114, 13118-13125.
196. N. K. Allam, A. J. Poncheri and M. A. El-Sayed, *ACS Nano*, 2011, 5, 5056-5066.
197. L. Xiang, X. Zhao, C. Shang and J. Yin, *J. Colloid Interface Sci.*, 2013, 403, 22-28.
198. R. Niishiro, R. Konta, H. Kato, W.-J. Chun, K. Asakura and A. Kudo, *J. Phys. Chem. C*, 2007, 111, 17420-17426.
199. Q. Gu, J. Long, L. Fan, L. Chen, L. Zhao, H. Lin and X. Wang, *J. Catal.*, 2013, 303, 141-155.
200. C. Su, L. Liu, M. Zhang, Y. Zhang and C. Shao, *CrystEngComm*, 2012, 14, 3989-3999.
201. G. Zhang, Z. Zhao, H. Tan, H. Zhao, D. Qu, M. Zheng, W. Yu and Z. Sun, *RSC Adv.*, 2015, 5, 21237-21241.

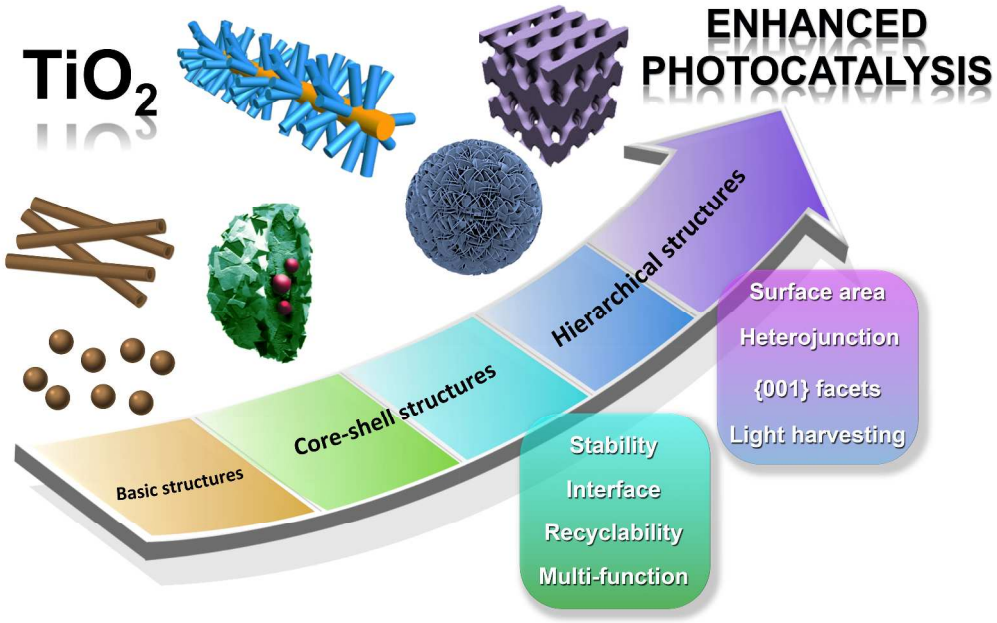

1783x1125mm (72 x 72 DPI)